Paleolatitude.org 3.0: a calculator for paleoclimate and paleobiology studies based on a new global paleogeography model

Short title: Paleolatitude 3.0: a calculator for paleoclimate and paleobiology studies

Douwe J.J. van Hinsbergen[1], Bram Vaes[2,3], Lydian M. Boschman[1], Nalan Lom[4], Suzanna H.A. van de Lagemaat[1], Eldert L. Advokaat[1], Sanne de Baar[1], Menno R.T. Fraters[5], Joren Paridaens[6], Emilia B. Jarochowska[1]

1. Department of Earth Sciences, Utrecht University, Utrecht, the Netherlands
2. Department of Earth and Environmental Sciences, Università degli Studi di Milano-Bicocca, Italy
3. Aix-Marseille Université, CNRS, IRD, INRAE, CEREGE, Aix-en-Provence, France
4. Department of Earth and Environmental Sciences, University of Central Asia, Khorog, Tajikistan
5. University of Graz, Department of Earth Sciences, Graz, Austria
6. 9de Online, Utrecht, the Netherlands

Corresponding author: Douwe van Hinsbergen, d.j.j.vanhinsbergen@uu.nl

*** This is a non-peer-reviewed preprint submitted to EarthArXiv. The manuscript has been submitted for publication in PLoS One***

Abstract

Paleogeography, and particularly the paleolatitude, provides key context in the interpretation of paleoclimatic and paleobiological data but these fields are typically studied by scientists in different disciplines. To facilitate communication between these disciplines, a decade ago the online Paleolatitude.org calculator was developed. This provided for any coordinate on stable tectonic plates a paleolatitude estimate for any chosen Phanerozoic time interval, including an uncertainty that includes paleogeographic uncertainty and age uncertainty of a sample/fossil. Here, we provide a major update to this tool. First, we include in the calculator the first global paleogeographic model, including GPlates reconstruction files, back to 320 Ma that also restores paleogeographic units that are now thrusted over each other in orogenic (mountain) belts. Second, we include a recent, more precise paleomagnetic reference frame with updated statistical procedures, and provide the first update of its underlying database. Third, we introduce a new online interface with an easy-to-use tool with a batch option, and data and graph export functions. Finally, we illustrate differences with previous reconstructions and show an application by calculating a paleolatitudinal biodiversity gradient for the late Jurassic in which we use a bootstrap approach to propagate paleolatitude and age uncertainty into the result.

1. Introduction

The study of paleoclimate, paleoceanography, and paleobiology depends for an important part on the interpretation of rocks and fossils, or geochemical tracers therein. However, these rocks and fossils are generally displaced relative to the location at which

46 they were deposited. As a result of plate tectonic motions, as well as episodes of wholesale
47 rotations of the solid Earth (crust and mantle) known as true polar wander [1], the
48 distribution of oceans and continents relative to each other and relative to the Earth's spin
49 axis continuously changed throughout geological time. Interpreters of paleoclimate, -
50 oceanography, and -biology need to take these changes into account, for which they rely on
51 paleogeographic reconstructions [2-5]. Such reconstructions, however, are typically made
52 by a different scientific community - those studying plate tectonics and geodynamics - and it
53 has proven to be a challenge to optimize communication between communities to ensure
54 that the latest state-of-the-art is available for multidisciplinary research.
55 An important quantitative parameter that is provided by paleogeographic
56 reconstructions is paleolatitude. Latitude, relative to the Earth's spin axis, determines the
57 angle of solar insolation and thus climate (bearing in mind that the Milankovitch cycles
58 caused by obliquity and precession modify solar insolation on ~20-40 kyr timescales). To
59 allow a user-friendly estimation of paleolatitude, the online paleolatitude calculator of
60 Paleolatitude.org was developed about a decade ago [6], which has since become a widely
61 used tool in the study of paleoclimate and paleobiology studies [7-11]. The paleogeographic
62 model behind that calculator, as well as the functionality of the calculator has now
63 undergone some significant improvements.
64 In this contribution, we describe the upgrade of Paleolatitude.org to version 3.0. First,
65 we upgrade to a fully-global paleogeographic model (dubbed the Utrecht Paleogeography
66 Model), updated to comply with data published since 2015 on marine magnetic anomalies
67 that describe the motions of major tectonic plates, and we have converted all ages to the
68 most recent geological timescale [12]. We also integrate detailed regional kinematic
69 reconstructions of rock units that are found in deformed orogenic belts such as in the

Mediterranean region, Iran, Himalaya and Tibet, SE Asia, the Caribbean region, and of continental fragments that make up present-day Mongolia, China, and Indochina. In addition, Paleolatitude 3.0 uses a novel global paleomagnetic reference frame for the last 320 Ma based on a global apparent polar wander path (gAPWP) that is based on an improved statistical analysis that stays closer to the original data and that significantly decreases paleogeographic uncertainty [13]. In this paper, we provide the first upgrade of the paleomagnetic database behind that gAPWP, upgrading from gAPWP23 to gAPWP25. We provide a brief synopsis of global paleogeography since late Carboniferous Pangea and provide the GPlates-based [14] global plate model files of the Utrecht Paleogeography Model. Additionally, we describe the improved functionalities of the Paleolatitude.org online tool, which include batch calculations for large datasets and the quantification of paleolatitudinal uncertainty for each sample. Finally, we compare the results of Paleolatitude.org with other widely used models and illustrate the use our updated tool with example applications on paleobiological datasets.

2. Methods and innovations in paleolatitude reconstruction

The main tool to quantitatively estimate the paleolatitude of a rock is paleomagnetism: the study of the Earth's magnetic field stored in rocks. The Earth's magnetic field is represented by field lines that, in a normal (or: reversed) field, point vertically out of (or: into) the Earth on the south pole, are horizontal pointing northward (or: southward) on the equator, and point vertically into (or: out of) the Earth at the north pole. Measuring the magnetic field stored in rocks thus provides a direct measure of the absolute paleolatitude at which it formed (provided that known sources of bias, scatter, and error are considered and

corrected for [15, 16]). However, as paleomagnetic data are not available for rocks of every age and every location, paleogeographic models use global plate reconstructions of relative plate motions that are placed in a global paleomagnetic reference frame [6, 17-20] (Figure 1).

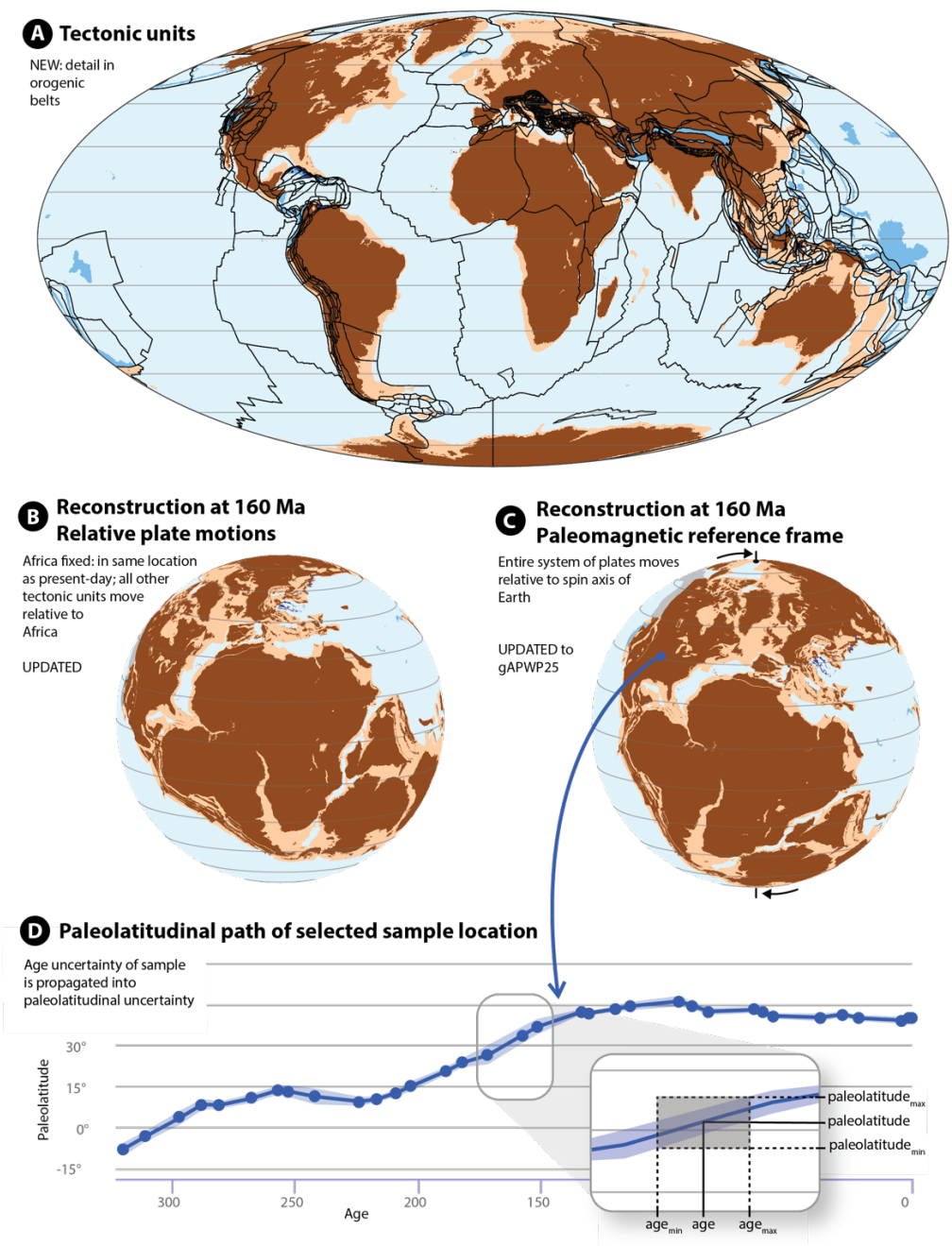

Figure 1: Plate and paleogeographic reconstruction approach underlying the Paleolatitude.org calculator

With major plates being essentially rigid (i.e., internally not significantly deforming), the relative positions of major plates that are separated by ocean basins may be reconstructed from marine magnetic anomalies and fracture zones on the ocean floor [21]. Such reconstructions have typical uncertainties in the order of tens of kilometers [22]. Plates separated by ocean basins collectively form a global plate circuit [21, 23]. This way, paleomagnetic data from one plate also constrain the position of all other plates in the plate circuit. All paleomagnetic data from plates connected in a global plate model may thus be used to collectively determine the paleoposition of the whole plate model relative to the spin axis, forming a global paleomagnetic reference frame [13, 24-28]. The Paleolatitude.org tool used such plate models placed in a global paleomagnetic reference frame to predict the paleolatitude of any coordinate within the plate circuit, through time [6].

The original paleolatitude calculator Paleolatitude.org 1.0 [6] included three global paleomagnetic reference frames, each with the plate model that was used to compute the reference frame: the frame of Besse and Courtillot [24] for 0-200 Ma, the frame of Kent and Irving [26] for 50-220 Ma, and the frame of Torsvik et al. [27] for 0-320 Ma. In a subsequent upgrade to Paleolatitude.org 2.0, detailed in an online comment on the original paper [29], the calculator was extended to the early Paleozoic for the major continents, based on the spline-fitted apparent polar wander paths for pre-Pangean continents computed in Torsvik et al. [27].

In addition to plate motions of the rigid major plates, the geological record contains widespread evidence for distributed deformation. Such deformation includes extension (rifting), and shortening (orogenesis). Rock units of such deformed belts, including all

mountain ranges of the Alpine-Himalayan belt and subduction-related fold-thrust belts of the circum-Pacific region were not yet included in the calculator. The underlying reason was that such reconstructions have additional and poorly quantifiable uncertainties. The paleoclimatic community, which was the target audience of the original calculator, tends to concentrate on rock records from stable plate interiors instead, e.g. from deep marine or passive margin shelf drill cores. However, those orogenic belts, which typically consist of deformed, sedimentary rocks offscraped from subducted oceanic plates or passive continental margins, provide far better outcrop access to geological records than most stable plate interiors do and these belts thus provide a rich paleontological record. In the last 15 years, detailed kinematic reconstructions of the orogenic belts have become available, especially because of the availability of GPlates open access plate reconstruction software [14]. This makes it now possible to upgrade Paleolatitude.org to include detailed reconstructions of orogenic belts.

In addition to developments in plate reconstructions, a new paleomagnetic reference frame for the last 320 Ma was developed [13]. The three frames that were included in the previous version of Paleolatitude.org all used the same underlying statistical approach, in which a series of paleopoles determined from stable plate interiors were averaged to form a global reference frame. The differences between the three frames thus stem from subtle differences in the underlying plate circuit reconstruction, and in the compilation of paleomagnetic poles used to compute the reference frame. However, the classical approach in paleomagnetism to combine paleomagnetic data into study-level poles, which contain an arbitrary number of data points, led to several flaws in the paleomagnetic quantification of relative tectonic motions [30], including irreproducibility and inflation of uncertainty [31]. Removing the arbitrary level of paleomagnetic poles and

computing the global paleomagnetic reference frame at the site-level instead [31] gives equal weight to each individual measurement of the past magnetic field and led to gAPWP23 [13], which has much smaller uncertainty and higher reproducibility. Paleolatitude.org 3.0 thus uses this paleomagnetic reference frame as default. In addition, we here provide the first post-publication upgrade of the underlying dataset of this reference frame as explained in section 4.

3. Plate and orogen reconstruction approach

The new default reconstruction in Paleolatitude.org 3.0 uses a global plate model that is based on marine magnetic anomalies and fracture zones of the modern ocean floor. The plate model underlying Paleolatitude 3.0 is the same as computed for the gAPWP23 paleomagnetic reference frame [13], updated with recently improved rotation poles for the Nazca relative to the Pacific Plate [32]. This plate circuit differs in details from the one underlying the APWPs used in the Paleolatitude 1.0 and 2.0: it includes more detailed reconstructions of ocean basins provided by the marine geophysical community in the last decade [33-36], and the age of all anomalies follows the latest geological timescale [12]. We refer the reader to the publication detailing gAPWP23 [13] for further details on the global plate model.

Besides regional reconstructions of orogenic belts, there is an increasing number of detailed reconstructions available of intra-plate rifting, i.e. the process of continental extension that precedes oceanic spreading and which may develop small microcontinental blocks adjacent to major continents [37-39]. Our global reconstruction incorporates reconstructions of microcontinental blocks but has not incorporated all details of

reconstructions of rifting from passive margins yet. For some margins, such reconstructions are available [37, 40] and they may be incorporated in future updates. Typical pre-break-up extension amounts ~150 km per passive margin [28], meaning that pre-extensional paleolatitudes of rocks on distal passive margins in our reconstructions may be up to 2° off if rifting had a N-S component.

Orogenic belts are regions where crust and lithosphere deformed, and where the hypothesis of plate rigidity that underlies plate reconstructions fails. Those belts contain rock units that have moved relative to their stable neighboring plates, and a much larger level of detail is needed to restore paleolatitude. Orogenic belts are in this reconstruction categorized in two classes: 'intraplate' orogens, that result from shortening of full lithospheric sections, and 'accretionary' orogens that consist of rock units offscraped from lithosphere that disappeared into the mantle by subduction [41].

Intraplate orogens, such the Andes, the Rocky Mountains, the Tibetan Plateau, the Tien Shan, or the Atlas Mountains, are regions where lithosphere was compressed, and crust was thickened and uplifted. The amount of deformation is typically limited - the largest intraplate shortening was restored in the Tibetan Plateau, and amounts to ~1000 km [42], whereas the Andes only recorded up to ~400 km [43, 44], and the Atlas only accommodated some tens of kilometers of shortening [45]. Intraplate deformation may also be extensional, for instance in back-arc basin settings, where previously thickened orogens may be stretched, such as in the Aegean region [46], the Basin and Range province [47], or the Sea of Japan [48]. Because back-arc basins often form from previously thickened orogenic crust, they may accommodate more continental extension before oceanic spreading than continents - for instance, the Aegean and Basin and Range regions already experienced ~400 km of extension and no oceanization has started yet [47, 49].

194 Continental intraplate deformation may thus move rock units relative to stable plate
195 interiors by a few degrees, and in extreme cases up to ~10°. We reconstruct such motions
196 using a reconstruction protocol that uses structural geological, stratigraphic, and
197 geochronological evidence to reconstruct (i) extensional deformation, which achieves its
198 largest geological record at the end of the deformation and is thus the most complete; (ii)
199 displacement along strike-slip faults, whereby the motion direction is well-constrained but
200 uncertainty may exist on the amount and timing of motion, and (iii) shortening deformation,
201 whereby the least complete geological record is achieved at the end of deformation and
202 only a minimum estimate of shortening may be made, of which the direction of shortening
203 may also have uncertainty. Subsequently (iv) a reconstruction is made that is geometrically
204 feasible without violating constraints, that is (v) tested against and if necessary iterated
205 within the constraints of steps (i) to (iii) based on paleomagnetic data that demonstrate
206 paleolatitudinal and vertical axis rotations [50, 51].
207 Oceanic crust may also undergo deformation, especially in oceanic subduction-zone
208 settings, but this deformation is typically more confined than in continental crust.
209 Contractional deformation is typically restricted to weak crust of volcanic arcs in the upper
210 plate of subduction zones [52]. Extensional deformation in upper oceanic lithosphere is
211 common, e.g. in the Scotia Sea region [53, 54], the Caribbean Plate [55] or in the Philippine
212 Sea Plate [56] and often leads to formation of microplates separated by back-arc basin
213 ridges. In addition, forearc slivers may form that displace upper plate oceanic or arc
214 fragments relative to stable plate interiors [57]. Reconstruction of this type of deformation
215 follows similar protocols as for deformed upper plate continental crust.
216 The preservation potential of upper plate oceanic lithosphere in the geological
217 record is limited: eventually, it will subduct. An exception is oceanic lithosphere of the

forearc, close to the plate contact. When accretionary prisms form below oceanic overriding plate lithosphere, or when continental margins arrive in a trench, the oceanic forearc may become uplifted and be protected from later subduction. Such uplifted, or 'obducted' oceanic forearcs then become preserved as ophiolites [58, 59]. Those ophiolites are often associated with deep-marine, pelagic oozes that hold important geological records of past oceanography, and our reconstruction has included their pre-obduction plate motion history to unlock such potential for global oceanography and planktonic biogeography. Key examples of orogens rich in obducted ophiolites include the Balkans, Cyprus, Anatolia, and Oman [60-63], the Philippines [64], New Guinea and New Caledonia [65], Cuba [66], and California [67], among many other examples.

Rock units in accretionary orogens may have travelled far larger distances relative to stable plate interiors. Accretionary orogens consist of rock units that were once part of now-subducted plates, and that were offscraped at subduction zones and accreted to upper plates, escaping subduction. Such accretionary orogens include the Pyrenees, Alps, Apennines, Dinarides, Hellenides, or Taurides in the Mediterranean region [68-71], the Zagros mountains in Iran [72], the Himalaya [73], large parts of SE Asia [74-76] much of Japan [77] and New Zealand [78], South Alaska [79] or California [67].

Rocks that accreted in such orogens may be derived from oceanic lithosphere, in which case they contain a history from the formation at a mid-oceanic ridge to the accretion into the orogen at a subduction zone [80]. Alternatively, they may be derived from continental lithosphere - typically passive continental margins or microcontinents. In that case, the accreted slices may contain a basement that underwent an earlier orogenic history, and a sequence that represents continental rifting, a passive margin evolution, and the accretion to an orogen when the continental margin went down into a trench [41].

Reconstructions of accretionary orogens first restore post-accretion intra-plate deformation [49], and subsequently reconstruct accreted rock units as part of the original downgoing plate prior to the moment of accretion. The maximum age of accretion is provided by the deposition of a coarsening-upward clastic sedimentary series derived from the upper plate (flysch, molasse) in the top of the stratigraphic sequence of the accreted unit, which marks the arrival of the units in a foreland basin/trench. The minimum age is determined by the oldest metamorphism, magmatism, contractional deformation, or upper plate sedimentation (i.e., forearc basin sedimentation [81]) that affected the unit and that indicates that it had become part of the upper plate [41, 82]. This time interval is typically constrained within a few million years and depending on the rate of convergence between the adjacent plates, may add a few degrees of uncertainty to the reconstructed position of an accreted unit on the original downgoing plate.

Importantly, none of the reconstruction protocols included any paleoclimatic, paleoenvironmental, or paleobiological interpretations. The reconstructions selected for Paleolatitude.org 3.0 provide independent paleogeographic input for such studies without introducing circular reasoning.

All kinematic reconstructions were made in GPlates plate reconstruction software [14] and the global plate reconstruction underpinning the Paleolatitude.org 3.0 model is provided in the Supplementary Information. In basin and orogen reconstructions, area change occurs due to deformation. For the paleolatitude calculator we divide such deforming regions in rigid polygons that may partly overlap (when extension is reconstructed) or be separated by gaps (when shortening is reconstructed) when reconstructed backwards in time. This division into polygons is an obvious, but practical, simplification and adds to the uncertainty of the region. However, for intensely deformed

266 regions, we used polygons on the scale of tens of kilometers (yielding thousands of polygons
267 in the model) and overlaps rarely exceed 100 km (i.e. max ~1° in paleolatitude) (Figure 1).
268 Polygons in orogens encompass rock units with a common paleogeographic origin, which
269 are bounded by faults. Polygons are typically pre-orogenic stratigraphic sequences that
270 were incorporated in orogens as major thrust slices, called nappes. These may have become
271 deformed, metamorphosed, intruded by magmatic rocks, and subsequently overlain by
272 sedimentary basins. Each polygon in an orogen is named after the nappe or tectonic block it
273 represents. Younger magmatic rocks or sedimentary basins are reconstructed with the
274 nappes they intrude or overlie and are not marked as separate polygons.

275 Despite the detail in the reconstructions of orogenic belts, simplifying their
276 geological complexity is inevitable. The true spatial distribution and geological structure of
277 rock units, as seen on a geological map cannot be fully captured into a global 2D model. In
278 most cases, this will not significantly affect the estimation of the paleolatitude of a specific
279 site. We acknowledge, however, that due to small georeferencing errors, we may have
280 misplaced tectonic boundaries by a few kilometers, which would cause a coordinate to fall
281 in a wrong polygon, in which case an incorrect paleolatitude may be provided. Similarly,
282 inaccuracies in sampling locations of a fossil or rock from an orogenic belt may place them in
283 an incorrect tectonic unit. Such potential errors are typically not more than a few degrees
284 but need to be considered when using the reconstruction.

285 The reconstruction uses a series of regional tectonic reconstructions of intraplate
286 deformation, back-arc basin development, and accretionary orogenesis, including of the
287 Scotia Sea [83]; the Andes mountains [44], the Caribbean region [50, 84], the western
288 United States [47, 85], the Mediterranean region [49, 51, 86, 87], the Central Tethysides of
289 the Iran-Afghanistan [88, 89], Oman [90], the Tibetan Plateau and Himalaya [42, 91, 92], SE

290 Asia [75], the Junction region of the Pacific and Tethys realms around the Philippine Sea
291 Plate and the SW Pacific back-arc basins [93, 94], the NW Pacific and Bering Sea region [95,
292 96], and the China Blocks and the Tibetan and Sundaland terranes [18, 97-100]. A detailed
293 reconstruction of the Canadian Cordillera, Alaska, and pre-late Cretaceous NE Siberia
294 (Kolyma-Omolon) is not yet included because none is available that follows our
295 reconstruction protocol - such a reconstruction will be incorporated in a next upgrade of the
296 Paleolatitude.org tool. In the supplementary information of this paper, we provide GPlates
297 files of the rigid polygon model that underpins the Paleolatitude.org tool, and a
298 paleogeography version that shows the paleogeographic distribution of oceanic and
299 continental lithosphere of the Utrecht Paleogeography Model.
300

301 4. gAPWP25: Updated Paleomagnetic Reference Frame

302 Here, we provide the first update of the site-based global apparent polar wander path
303 (gAPWP) of Vaes et al. [13] for the past 320 Myr. This updated path, named *gAPWP25*, serves
304 as the new default paleomagnetic reference frame of Paleolatitude.org 3.0, and related
305 online tools including Paleomagnetism.org [101, 102] and APWP-online.org [103].
306 We made the following modifications to the paleomagnetic database that underlies
307 the site-level based gAPWP. First, we corrected typographical errors in entry names, sampling
308 locations, and other parameters. Second, we revised the ages of four North American
309 datasets according to constraints pointed out in recent compilations [104, 105]. All
310 modifications to the database are documented in the change log (Supplementary Files). We
311 further compiled all paleomagnetic poles published since 2022 that were obtained from rocks
312 younger than 320 Ma exposed in stable continental interiors. From this compilation, we

added 26 datasets that satisfy the selection criteria of Vaes et al. [13] to the global data compilation (Table 1). Sediment-derived datasets were accepted if they either meet the reliability criteria for inclination shallowing-corrected poles [106], receiving a reliability grade 'A' or 'B', or pass both the bootstrap reversal test of Heslop et al. [107] and the SVEI test of Tauxe et al. [108]. In addition, six datasets published prior to 2000 that satisfy the selection criteria were added, two of which were previously excluded in gAPWP23 [13] but are included following a positive SVEI and reversal test result. In total, 32 entries were added (~10%) to the database used to compute the updated global APWP. The complete database is provided in the Supplementary Files, and on APWP-Online.org, where also future further updates will also be logged.

name	Age_{min}	Age_{max}	age	Slat	Slon	N	K	A95	plat	plon	Rlat	Rlon	lithology	f	p_std	reference
Mt Ruapehu volcano, Aotearoa New Zealand	0	0.01	**0.005**	-39.3	175.6	**18**	59.1	4.5	**-85.1**	**77.5**	**-85.1**	**77.5**	igneous			a
Tres Vírgenes Volcanic Complex, Baja California, Mexico	0.02	0.30	**0.2**	27.5	-112.6	**12**	12.0	13.0	**-80.9**	**333.0**	**-80.9**	**333.1**	igneous			b
Trindade Island, offshore Brazil	0.06	0.8	**0.4**	-20.5	-29.3	**14**	12.2	11.9	**-79.1**	**267.4**	**-79.1**	**267.7**	igneous			c
Andacollo volcanics, Argentina	0.9	3.8	**2.4**	-37.2	-70.8	**17**	30.2	6.6	**-84.9**	**31.5**	**-84.5**	**33.2**	igneous			d
Caviahue-Copahue Volcanic Complex, Northern Patagonia	0.0	5.6	**2.8**	-37.9	-71.0	**42**	26.4	4.4	**-84.3**	**251.4**	**-84.7**	**253.6**	igneous			e
Eyjafjarðardalur basalts, Iceland	2.6	8.0	**5.3**	65.5	-18.8	**114**	11.9	4.0	**-82.0**	**5.0**	**-82.1**	**7.4**	igneous			f
Vogelsberg volcanics, Germany	15.2	17.6	**16.4**	50.5	9.2	**116**	18.2	3.2	**-84.5**	**341.9**	**-84.2**	**359.8**	igneous			g
Imnaha and Grande Ronde basalts, US	16.0	17.0	**16.5**	45.8	-116.8	**30**	15.0	6.8	**-85.0**	**335.0**	**-85.7**	**343.7**	igneous			h
Sleat Peninsula dykes, Isle of Skye, UK	53.9	61.7	**57.8**	57.00	-5.90	**24**	21.1	6.6	**-75.2**	**1.8**	**-69.4**	**32.0**	igneous			i
South Rewa Basin dykes, India	64.0	67.0	**65.5**	23.8	81.7	**13**	33.9	6.9	**-42.0**	**109.3**	**-77.3**	**66.3**	igneous			j
Uberaba Formation, Brazil	72.2	76.0	**74.1**	-19.8	-47.9	**120**	13.4	3.7	**-85.2**	**336.0**	**-75.1**	**51.3**	sedimentary	0.6	3.2	k
Alkaline dykes, Santos-Rio de Janeiro coast, Brazil	80.0	88.0	**84.0**	-23.9	-45.4	**44**	44.0	3.0	**-81.2**	**319.7**	**-70.8**	**43.2**	igneous			l
Okhotsk-Chukotka Volcanic Belt, Siberia	83.7	88.6	**86.2**	66.9	170.0	**57**	14.1	5.2	**-76.8**	**350.0**	**-67.6**	**45.5**	igneous			m
Granite Mountain, Arkansas, US	87.5	91.5	**89.5**	34.7	267.7	**5**	21.0	17.1	**-77.8**	**351.4**	**-70.5**	**49.6**	igneous			n
Ramon volcanics, Israel	112.6	119.1	**115.8**	30.5	34.7	**46**	35.6	3.6	**-57.2**	**72.3**	**-57.5**	**72.4**	igneous			o
Parana basalts - Gramado & Herveiras regions, Brazil	133.6	135.0	**134.3**	-29.4	-52.6	**37**	56.6	3.2	**-82.8**	**45.2**	**-48.3**	**81.1**	igneous			p
Puerta Curaco section, Tithonian, Neuquen, Argentina	143.1	149.2	**146.2**	-37.4	290.1	**27**	50.4	4.0	**-81.1**	**108.6**	**-49.0**	**91.7**	sedimentary	1.00	0.00	q
Notre Dame Bay dikes 2	146.1	150.0	**148.1**	49.5	304.9	**15**			**-73.9**	**21.0**	**-48.8**	**94.3**	igneous			r
Penatecaua Formation, Brazil	200.4	202.4	**201.4**	-3.0	-54.0	**30**	48.0	3.8	**-77.5**	**260.1**	**-63.1**	**59.7**	igneous			s
Mercia Mudstone Group (Haven Cliff), England, UK	205.0	212.0	**208.5**	50.7	-3.2	**74**	24.0	3.4	**-54.8**	**287.7**	**-66.0**	**53.2**	sedimentary	0.65	3.56	t
Mercia Mudstone Group (ML, SH, MB, SE), England, UK	212.0	224.0	**218.0**	50.7	-3.2	**83**	21.5	3.4	**-56.2**	**295.4**	**-63.6**	**55.5**	sedimentary	0.50	4.07	t
Mercia Mudstone Group (MS, MD, MW), England, UK	227.3	240.4	**233.9**	50.7	-3.2	**70**	29.0	3.2	**-51.4**	**308.2**	**-55.5**	**49.5**	sedimentary	0.85	2.21	t
Otter Sandstone Fm, Devon, England, UK	239.5	244.2	**241.9**	50.6	-3.3	**31**	20.1	5.9	**-55.2**	**326.0**	**-47.3**	**61.8**	sedimentary	1.00	0.00	u
Musschelkalk carbonates, Poland	237.0	246.7	**241.9**	50.0	19.5	**28**	65.4	3.4	**-51.0**	**323.0**	**-46.9**	**55.1**	sedimentary	1.00	0.00	v
Abinskaya Group, Siberian large igneous province	250.8	252.2	**251.5**	54.3	84.1	**33**	20.2	5.7	**-59.0**	**340.3**	**-42.3**	**71.6**	igneous			w
Nzalet el Lararcha, Morocco	276.5	277.7	**277.1**	32.3	352.4	**12**	30.4	8.0	**-49.8**	**45.3**	**-49.6**	**47.4**	igneous			x
Mechraa Ben Abbou, Morocco	284.0	292.8	**288.4**	32.7	352.2	**15**	45.8	5.7	**-45.1**	**41.5**	**-47.4**	**47.3**	igneous			x
Kenifra, Morocco	283.4	295.7	**289.6**	33.0	354.3	**12**	33.4	7.6	**-34.4**	**59.4**	**-45.0**	**43.4**	igneous			x
Tiddas, Morocco	281.7	295.1	**288.4**	33.6	353.8	**14**	42.9	6.1	**-47.6**	**45.3**	**-33.9**	**60.9**	igneous			x
Chougrane, Morocco	292.1	311.8	**302.0**	33.0	353.7	**12**	54.8	5.9	**-37.6**	**63.8**	**-37.0**	**65.4**	igneous			x
From Vaes et al. (2023) database																
Monteregian Hills intrusives	122.8	126.1	**124.5**	45.3	286.8	**70**	29.0	3.2	**-72.4**	**11.0**	**-52.1**	**81.1**	igneous			y
Heming limestone, France	237.0	246.7	**241.9**	48.7	7.0	**58**			**-54.3**	**320.6**	**-49.7**	**58.6**	sedimentary	1.00	0.00	z

Table 1: List of data that were added up of Vaes et al. [13] to upgrade to gAPWP25. For total database, see Supplementary Information, or apwp-online.org. Age_{min} and Age_{max} = lower and upper boundaries of age uncertainty range; Slat/Slon = latitude and longitude of (mean) sampling location; N = number of paleomagnetic sites used to compute the

paleopole; A95 = radius of the 95% confidence circle about the mean of the distribution of VGPs; K = Fisher [109] precision parameter of the distribution of VGPs; Plat/Plon = paleopole latitude and longitude (south pole); Rlat/Rlon = paleopole latitude and longitude in coordinate frame of South Africa; f = flattening factor (only for sedimentary data), pstd = standard deviation of the assumed normal distributed co-latitudes, obtained from E/I correction [110] (only for sedimentary data); Key to references: a = [111], b = [112], c = [113], d = [114], e = [115], f = [116], g = [117], h = [118], i = [119], j = [120], k = [121]; l = [122], m = [123], n = [124]; o = [125]; p = [126]; q = [127], r = [128], s = [129], t = [130], u = [131], v = [132], w = [133], x = [134], y = [135], z = [136]

The updated global APWP was computed using the approach described in Vaes et al. [13] and is provided in coordinates of South Africa in Table 2 (for versions in the coordinates of other major continents, see the Supplementary Files). The gAPWP25 shows only minor differences with its predecessor gAPWP23 (Figure 2). The largest angular differences (~1.5°-2.5°) are observed for three time intervals: the Late Cretaceous, latest Jurassic and Early Triassic (Figure 2). These intervals are characterized by relatively low data density, which increases the influence of newly added datasets. Nevertheless, all reference poles of gAPWP25 have overlapping 95% confidence regions with those of gAPWP23. Likewise, estimated APW rates show no significant changes. Absolute plate motions in the paleomagnetic reference frame, and estimated changes in paleolatitude over time, will therefore remain very similar to those predicted by gAPWP23, albeit with slightly smaller uncertainties due to the increased amount of data. The paleomagnetic reference frame can be used for any global or regional plate reconstruction in the GPlates software [14] by adding total reconstruction poles provided in Table 3 to the rotation file. A ready-to-use rotation file

is included in the Supplementary Files, which ties South Africa (plate ID 701) to the spin axis (plate ID 001) for the past 320 Myr.

Window	Age	N	P95	Longitude	Latitude	Mean K	Mean CSD	Mean E
0	1.4	1960.2	0.7	324.3	-89.3	18.8	18.7	1.06
10	4.6	2915.0	1.2	346.8	-87.8	17.8	19.2	1.08
20	21.5	1261.9	1.1	12.5	-82.7	17.3	19.5	1.08
30	28.2	1087.8	1.0	23.3	-80.8	18.0	19.1	1.08
40	37.5	475.2	1.4	26.0	-79.6	19.6	18.3	1.14
50	56.1	1119.3	1.0	31.1	-75.1	16.3	20.1	1.11
60	60.1	1744.2	0.8	35.3	-73.7	16.5	20.0	1.08
70	65.7	1029.5	1.3	40.5	-73.4	16.9	19.7	1.11
80	81.0	574.3	1.8	49.6	-72.5	21.8	17.4	1.13
90	88.8	524.9	1.3	60.7	-68.7	23.2	16.8	1.16
100	94.3	214.1	2.4	71.6	-64.3	22.6	17.1	1.22
110	115.1	300.3	1.4	79.5	-57.8	30.1	14.8	1.23
120	120.3	568.2	1.1	79.4	-55.0	29.2	15.0	1.15
130	130.7	895.1	0.8	82.4	-50.8	33.5	14.0	1.09
140	135.2	706.6	0.9	84.6	-49.8	35.7	13.6	1.12
150	151.0	196.4	2.2	86.6	-51.9	20.5	17.9	1.23
160	158.7	149.0	3.1	83.2	-55.8	14.7	21.2	1.23
170	172.6	112.0	3.6	78.8	-59.0	14.7	21.2	1.29
180	182.1	319.3	1.7	79.5	-64.2	19.0	18.6	1.29
190	189.7	470.1	1.5	75.3	-65.8	18.9	18.7	1.18
200	203.8	1482.2	1.7	62.9	-65.3	12.7	22.7	1.09
210	209.7	2446.5	1.3	58.0	-63.0	15.2	20.8	1.07
220	217.5	1700.9	1.1	53.9	-59.8	22.1	17.2	1.07
230	225.9	670.2	1.5	53.1	-56.5	23.3	16.8	1.11
240	241.3	387.9	1.9	57.4	-48.6	18.5	18.8	1.18
250	252.4	1139.1	1.9	61.8	-43.2	14.2	21.5	1.10
260	257.0	1233.0	1.7	62.6	-42.1	15.6	20.5	1.10
270	268.7	645.7	1.7	58.4	-41.1	26.4	15.8	1.15
280	281.4	844.6	1.3	56.8	-37.8	29.6	14.9	1.24
290	288.4	795.1	1.9	57.7	-35.5	29.7	14.9	1.15
300	297.8	427.4	2.5	52.4	-31.3	24.8	16.3	1.27
310	311.0	375.7	2.6	45.7	-26.8	18.4	18.9	1.40
320	320.2	428.5	2.7	39.9	-28.3	13.5	22.0	1.34

Table 2. Global apparent polar wander path of Vaes et al. [13] upgraded to gAPWP25 using the additional data shown in Table 1, calculated using a 20 Ma sliding window. For each window, the mean age of the re-sampled VGPs in that window is provided. N and P95 are the average number of re-sampled VGPs that fall within the time window and the 95%

confidence region of the reference pole (in degrees). Mean K, CSD and E are the average [109] precision parameter, circular standard deviation, and elongation of the re-sampled VGPs, respectively.

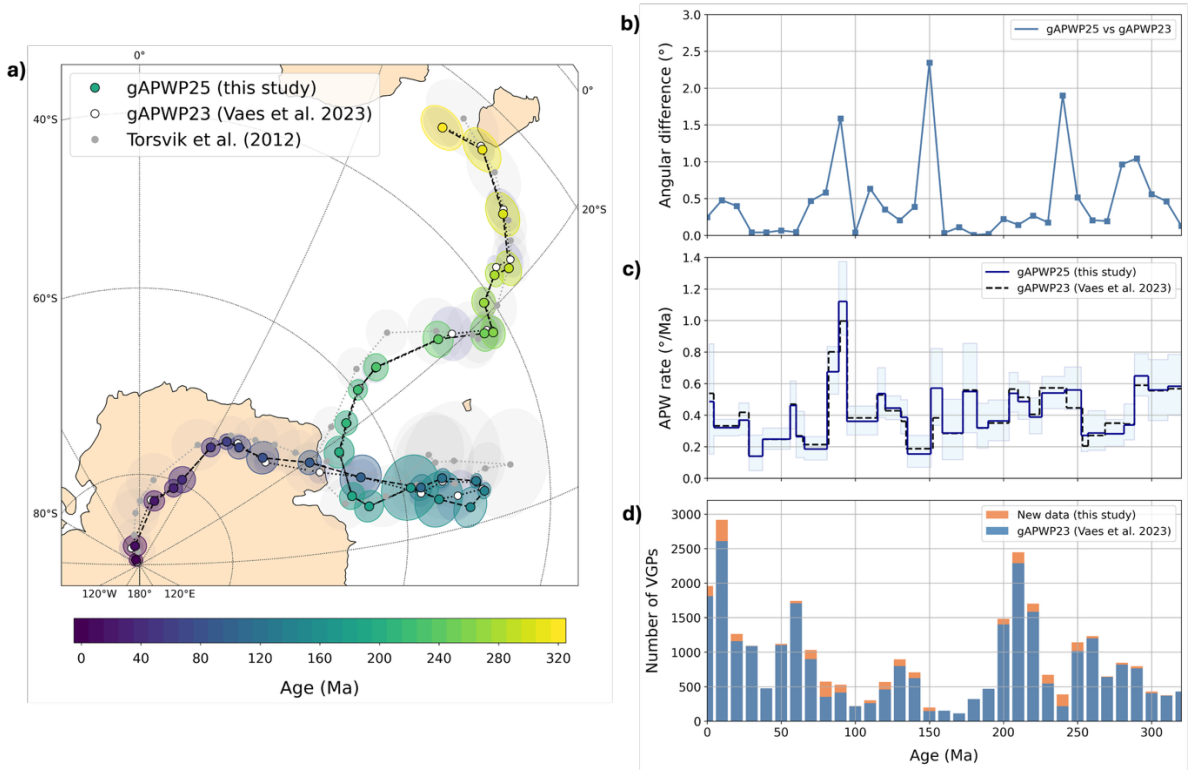

Figure 2: Global apparent polar wander path of Vaes et al. [13] upgraded to gAPWP25, using the additional data listed in Table 1. For the new APWP and the associated paleomagnetic reference poles, see Tables 2 and 3, respectively.

PlateID	Age	Euler_lat	Euler_lon	Euler_ang	Fixed plateID
701	0	0	90	0	1
701	1.4	0	54.3	0.7	1
701	4.6	0	76.8	2.2	1
701	21.5	0	102.5	7.3	1
701	28.2	0	113.3	9.2	1
701	37.5	0	116.0	10.4	1
701	56.1	0	121.1	14.9	1
701	60.1	0	125.3	16.3	1

701	65.7	0	130.5	16.6	1
701	81.0	0	139.6	17.5	1
701	88.8	0	150.7	21.3	1
701	94.3	0	161.6	25.7	1
701	115.1	0	169.5	32.2	1
701	120.3	0	169.4	35.0	1
701	130.7	0	172.4	39.2	1
701	135.2	0	174.6	40.2	1
701	151.0	0	176.6	38.1	1
701	158.7	0	173.2	34.2	1
701	172.6	0	168.8	31.0	1
701	182.1	0	169.5	25.8	1
701	189.7	0	165.3	24.2	1
701	203.8	0	152.9	24.7	1
701	209.7	0	148.0	27.0	1
701	217.5	0	143.9	30.2	1
701	225.9	0	143.1	33.5	1
701	241.3	0	147.4	41.4	1
701	252.4	0	151.8	46.8	1
701	257.0	0	152.6	47.9	1
701	268.7	0	148.4	48.9	1
701	281.4	0	146.8	52.2	1
701	288.4	0	147.7	54.5	1
701	297.8	0	142.4	58.7	1
701	311.0	0	135.7	63.2	1
701	320.2	0	129.9	61.7	1

Table 3. Paleomagnetic reference frame based on the updated gAPWP25 [13], rotating South Africa (701) into the coordinates of the Earth's spin axis (001). See Supplementary Information for a version in GPlates .rot file format.

5. A brief synopsis of global paleogeography since the Carboniferous

Earth's changing paleogeography may at first order be described in the terminology used for supercontinents: a dispersing set of continents that enclose an internal ocean (the Tethys), and that consume an external ocean (the Panthalassa or Paleo-Pacific) [137, 138]. Most of the modern continental crust, except Siberia (until ~250 Ma ago) and the China Blocks (until ~140 Ma ago) [18, 100] was joined together in the Late Carboniferous and

Permian in the supercontinent Pangea. This is the oldest part of the global reconstruction covered by our paleolatitude calculator. From the Jurassic onwards, the continents dispersed by the opening of the Atlantic Ocean and associated proto-Caribbean and Alpine Tethys oceans, as well as the Indian and Southern Oceans (Figure 3). The opening of the Atlantic Ocean and western Southern Ocean occurred at the expense of the external, Panthalassa Ocean. Lithosphere of this ocean basin was consumed at circum-Panthalassa subduction zones and remains of these plates are now found in the circum-Pacific accretionary orogens. The opening of the Indian and eastern Southern Oceans occurred at the expense of the internal, Tethys Ocean, which closed and formed the Alpine-Himalayan-Indonesian accretionary orogen (Figure 3).

The exterior, Panthalassa Ocean consisted mostly of oceanic plates that spread relative to each other and were consumed at subduction zones, both intra-oceanic [139-142], as well as along the margins of the Pangea continents North and South America, Antarctica, Australia as well as Siberia and the China Blocks. Back in time, the modern plates underlying the Pacific Ocean covered an increasingly smaller area. The remaining area was mostly occupied by oceanic lithosphere that has since been lost to subduction. Geological remains of these 'lost' Panthalassa plates consist of remnants of formerly intraoceanic subduction zones and fragments of plates that were trapped between or adjacent to continents, rock units that broke off circum-Panthalassa continents and were later re-accreted, and accretionary prisms offscraped of Panthalassa lithosphere. Examples of the latter are the earlier mentioned records of accretion in the orogens of New Zealand, Japan, Alaska, and California. These records are often sparse or so narrow that we have not reconstructed these in detail yet.

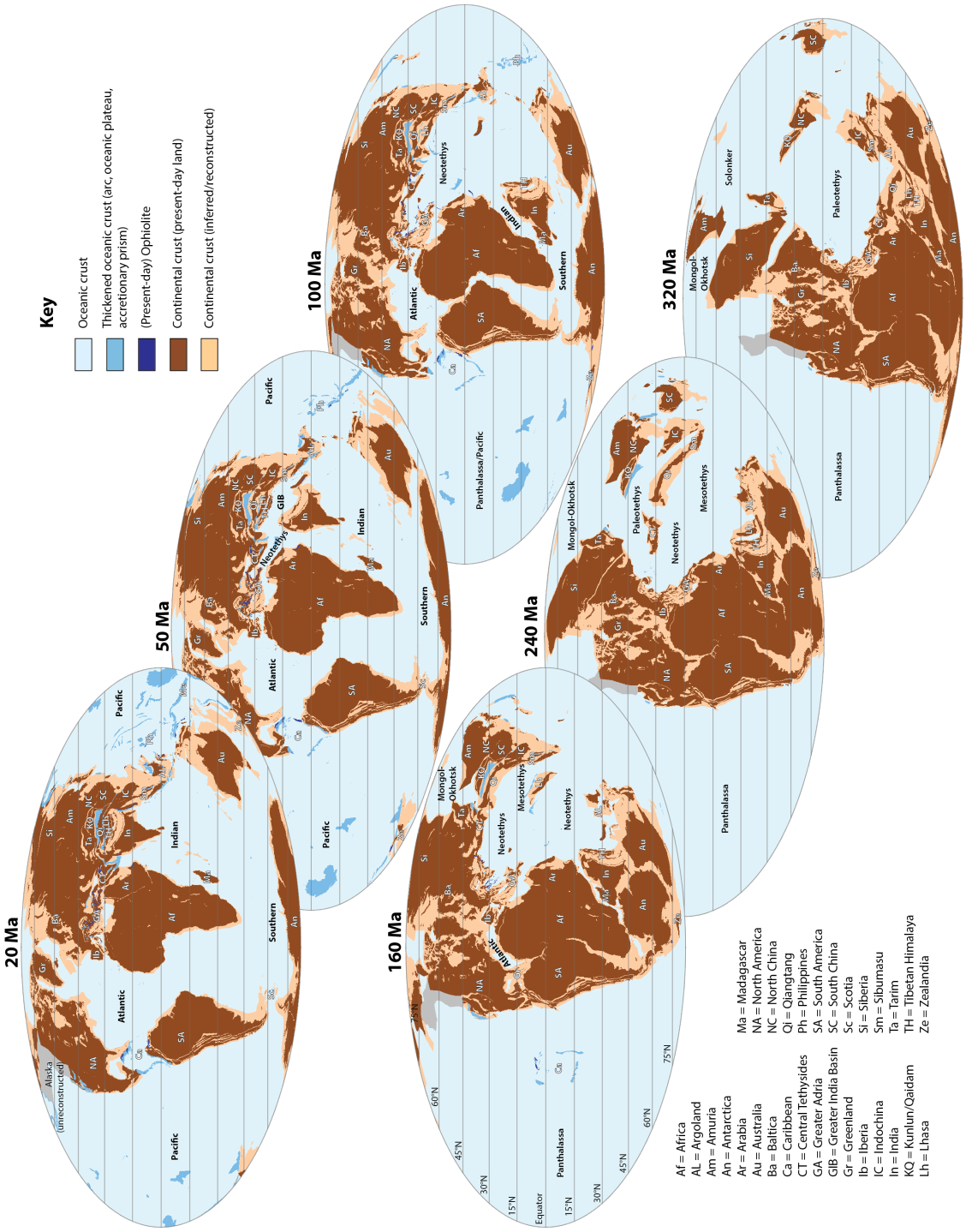

Figure 3. Global paleogeography snapshots of the Utrecht Paleogeography Model that shows the distribution of continental and oceanic crust, placed in the paleomagnetic reference frame based on gAPWP25 [13] (Table 2). The associated GPlates files are provided in the Supplementary Information.

406 Examples of trapped oceanic lithosphere include the modern Caribbean Plate and
407 circum-Caribbean accreted arc fragments now exposed in e.g. Colombia, Venezuela, Cuba,
408 and Nicaragua, which are fragments of the Jurassic Farallon plate [50, 143-145]. The
409 Aleutian Basin in the Bering Sea region likely contains Cretaceous back-arc basin crust that
410 formed above an intra-oceanic subduction zone whose arc remains are now found on
411 Kamchatka, the circum-Sea of Okhotsk region, and northern Japan [95]. This piece of
412 oceanic lithosphere likely became trapped between Alaska and Siberia upon initiation of the
413 Aleutian subduction zone at ~55-50 Ma (Figure 3).
414 Arc or continental fragments that became separated from the Panthalassa margins
415 through formation of back-arc basins are now prominent in the SW Pacific region, where the
416 continent of Zealandia broke off Antarctica and Australia, and back-arc basins formed
417 between Zealandia and the Pacific realm [94, 146, 147] (Figure 3). Similar systems
418 (de)formed and displaced the circum-Philippine Sea plate records as well as ophiolite
419 complexes of New Guinea and the Philippines [93, 148, 149]. The Cordilleran orogen of
420 western North America likely underwent similar processes but its geological history remains
421 debated. Mexico hosts the remains of the Guerrero Arc that became separated and
422 reconnected with North America through the opening and closures of the Late Jurassic to
423 Cretaceous Arperos back-arc basin [150, 151]. Farther north in western Canada and Alaska
424 are records that also indicate systems like this, but as explained before, we have not
425 incorporated this region yet in our reconstruction and refer the reader to a selection of
426 publications [142, 152-157] that cover some of the many different views on NE
427 Panthalassa/Cordilleran history. The last region with widespread orogenic deformation in
428 the circum-Pacific region is the Scotia Sea region. This deformed belt formed by westward
429 subduction of Atlantic Southern Ocean lithosphere below South America and eastward

subduction of Pacific Southern ocean lithosphere below the Antarctic peninsula, rifting fragments off both continental overriding plates and dispersing these via opening of multiple small, oceanic back-arc basins since the Eocene [53, 54, 83, 158].

The paleogeography of the interior ocean of the Tethyan realm is in general more complex than that of the exterior ocean, due to the repeated rifting of continental fragments off one margin - often the southern - and their accretion to the other - northern - margin [159-161]. Particularly in the Permian and Triassic, the Pangea-Tethys system was essentially in a mode of self-subduction [162], whereby the consumption of oceanic lithosphere below one margin led to the break-up of the opposite margin, forming a new ocean basin whose growth was accommodated by subduction of the older ocean [162]. When Pangea started breaking up in the Jurassic, this mode of rifting on one side and collision on the other side continued, such that continental fragments migrated northward from the southern to the northern hemisphere over distances that increased towards the east [75, 92, 163]. Many of the orogens of the Alpine-Himalayan mountain belt contain remnants of such microcontinental fragments. The Alpine-Himalayan orogen is divided into E-W trending segments separated by ancient transform fault systems. These segments reflect the opening of ocean basins at different times. This is somewhat analogous to the modern Atlantic Ocean that is compartmentalized into four segments: the South Atlantic, formed by Cretaceous separation of Africa and South America; the Central Atlantic, formed in Jurassic time by separation of Africa from North America; the 'Iberian' Atlantic and Bay of Biscay, formed by Jurassic separation of Iberia from Newfoundland and Eurasia; and north Atlantic, formed by Cenozoic separation of Eurasia from North America/Greenland [23]. In the Neotethyan realm, the different segments of the plate boundary system coincide with the Mediterranean, Iranian, Tibetan, and SE Asian regions. The former two formed by

454 oceans opening and closing between Gondwana and Eurasia. For the latter two, multiple
455 Tethyan ocean basins opened and closed between Gondwana and the China blocks. The
456 China blocks only became part of Eurasia in the latest Jurassic or earliest Cretaceous [98,
457 164], adding further paleogeographic complexity, as summarized below (Figure 3).
458 A continental realm dubbed ‘Greater Adria’ [51, 165], roughly the size of Greenland,
459 occupied much of the area that intervened Africa and Eurasia in the Mediterranean realm.
460 Greater Adria broke off northern Gondwana (Africa), where it occupied the region between
461 the east Tunisian and Levant margins during the Triassic-Jurassic opening of the Eastern
462 Mediterranean ocean. It separated from Iberia and Eurasia by the opening of the Alpine
463 Tethys ocean that was linked to the opening of the Atlantic Ocean [166, 167], and it was
464 bounded in the northeast by the Neotethys Ocean. The latter opened during Triassic to
465 Jurassic time when ribbons of continental crust preserved in the Balkans and the Pontides
466 and Lesser Caucasus broke off northern Gondwana. These were transferred to the Eurasian
467 margin, closing the Paleotethys ocean in the north(east) and opening the Neotethys in their
468 wake in the south(west) [51, 168] (Figure 3). Such continental ribbons between a
469 'Paleotethys' and 'Neotethys' have been identified throughout the Tethyan realm and are
470 referred to as 'Cimmerian continents' [169], but the ages of opening of Neotethys and
471 Paleotethys vary between the segments identified above. Greater Adria was internally
472 strongly extended and mostly submarine and was covered by limestones whose deformed
473 remnants now make up the Apennines, southern Alps, Dinarides, Hellenides, and Anatolide-
474 Tauride mountain belts [51, 168, 170-172] (Figure 3). The Alps, Carpathians, and eastern
475 Balkans were derived from subducted Eurasian continental margin lithosphere [68, 173,
476 174].

To the east, the Iranian segment consists of a 'Cimmerian' microcontinental ribbon whose remains occupy much of Iran and north Afghanistan (Figure 3). However, Paleotethys closure and Neotethys opening on either side of this continent predated the Cimmerian history of the Mediterranean region: the Iranian Cimmerian bock broke off the Arabian margin in the late Permian and collided with Eurasia in the Late Triassic [169, 175-177]. In the Jurassic to Early Cretaceous, the Iranian Cimmerian block was broken in fragments by the opening of back-arc basins that subsequently closed in Late Cretaceous to Eocene time [88, 178]. In the Iranian segment, the Neotethys was a few thousand kilometers wide and subducted from the Jurassic until the Oligocene onset of Arabia-Eurasia collision [89, 179].

The Tibetan and Himalayan segment of the Neotethys has seen a series of microcontinents rifting off Gondwana and colliding with the North and South China Blocks (Figure 3). First, a continental ribbon rifted off Gondwana in the Late Carboniferous to Early Permian. This consisted of the Qiangtang terrane of Tibet (or terranes - some interpret multiple continental blocks that collided sometime in the late Paleozoic or early Mesozoic [180], which continued to the east (and at present, southeast) as the Sibumasu and west Sumatra terranes. The Indochina block, that presently occupies much of Thailand, Laos, Cambodia, and Vietnam, in turn broke off in this process from Sibumasu to open a narrow oceanic basin in its wake [181]. These blocks collided with South China and the Kunlun arc of northern Tibet, which was part of the North China Block, in the Late Triassic [99, 181-183]. This process closed the Paleotethys Ocean to the north and opened the 'Mesotethys' Ocean to the South. Subsequently, the Lhasa terrane, which likely started rifting from the Greater Indian and west Australian margin of Gondwana in the Late Carboniferous [184], drifted northwards between Late Triassic and Early Cretaceous time [185]. This closed the Mesotethys and opened the Neotethys Ocean. Late Carboniferous-Early Permian and Late

501 Triassic rifting also affected the western Australian margin [186] and separated continental
502 fragments that finally broke off in the latest Jurassic to form 'Argoland' [187]. This
503 microcontinental archipelago, together with the intra-oceanic Woyla arc, collided in
504 Cretaceous to Eocene time with Sibumasu and West Sumatra [75, 188]. During this process,
505 in early Cretaceous time, rifting started within the Greater Indian margin of north
506 Gondwana, reflected by a series of Lower Cretaceous rift-related volcanics found in the
507 northern, 'Tibetan' Himalaya [189]. Paleomagnetic data and tectonic reconstructions show
508 that the Tibetan Himalaya became separated from Greater India in the Cretaceous, and
509 drifted northwards to close the Neotethys ocean and opening a 'Greater India Basin' in its
510 wake [92] (Figure 3). This interpretation remains debated [190], but because our
511 reconstruction everywhere systematically follows paleomagnetic evidence, the calculator
512 does so for the Tibetan Himalayan terrane too. In the Early Cretaceous, also India broke off
513 Gondwana and started its northward journey, leaving microcontinents in its wake (e.g., west
514 of Australia [163, 191] and the Seychelles [192]) due to ridge jumps in the Indian Ocean. The
515 Greater India basin closed in the Eocene and Oligocene, after the Neotethys closed and
516 Tibetan Himalaya collided with southern Tibet around 60 Ma [193] and until the arrival of
517 the Indian continental margin in the latest Oligocene to middle Miocene [194].
518 The China Blocks to the north of the Tethyan oceans, however, were not part of
519 Eurasia until the latest Jurassic or earliest Cretaceous, when the Mongol-Okhotsk Ocean
520 closed [164]. This ocean opened in Permian time as a back-arc basin behind a subduction
521 zone that consumed ocean floor of the western Panthalassa Ocean, and that broke a
522 continental ribbon known as 'Amuria' from Siberia [164, 195]. The Mongol-Okhotsk Ocean
523 started closing again in the Late Triassic, when the North China Block collided with Amuria in
524 the south forming the Solonker Suture. The North China Block had broken off eastern

525 Gondwana in Devonian time [196], and gradually moved north until it collided with Amuria
526 in the Late Triassic. Around that same time, the South China Block, that also broke off
527 Gondwana in the Devonian [197], collided with North China [198]. After the Late Triassic,
528 the China Blocks together with the Tibetan terranes became a single continent that moved
529 north towards Siberia, becoming part of Eurasia following Mongol-Okhotsk closure (Figure
530 3).
531

532 6. New online interface and functionality

533 The Paleolatitude 3.0 online tool is available on www.paleolatitude.org and provides two
534 options to compute paleolatitudes. On the home screen, any location may be chosen on the
535 map by a mouse click, and a graph will appear showing the paleolatitudinal evolution of that
536 location since 320 Ma (or shorter, if the selected location is part of an oceanic plate or
537 polygon that formed after 320 Ma). A maximum of ten curves may be computed at a time
538 (Figure 4). The graph can be downloaded as various figure formats, including as a vector
539 image and the underlying calculated paleolatitudes and their uncertainties can be
540 downloaded as an Excel file.
541 The home screen contains a button that opens a page with Advanced options. At the top, a
542 list of previously mouse click-selected locations is provided, to which the user may manually
543 add locations with a specified latitude and longitude, and if desired, a specific age or age
544 range (Figure 4). In addition, the user may choose the preferred paleomagnetic reference
545 frame. The default is the frame is Vaes et al. [13], with indication of the version of the
546 underlying dataset. At the time of writing, this is version gAPWP25, which is attached as
547 appendix to this paper. Future updates will be indicated on the Paleolatitude.org website,

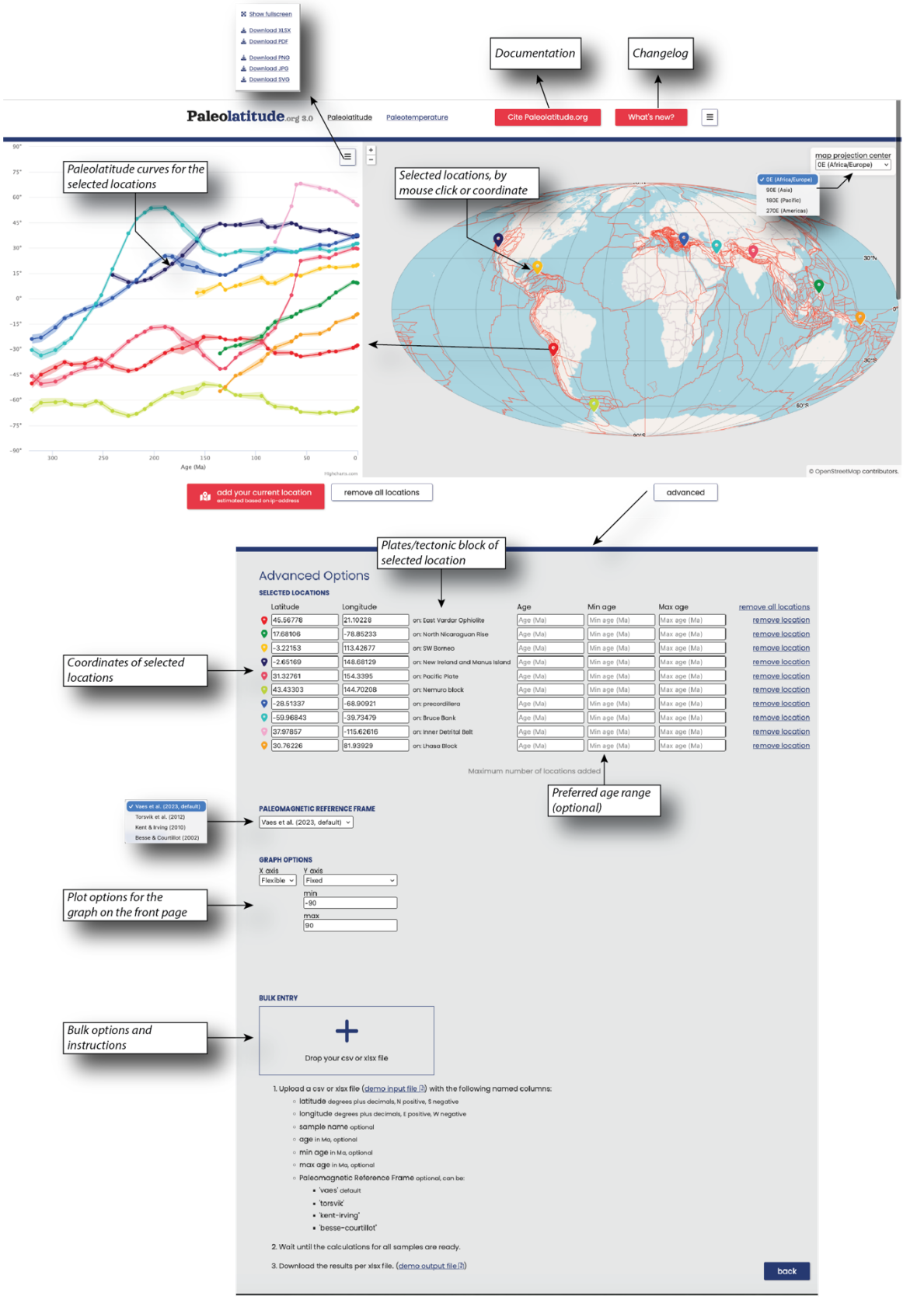

Figure 4. Outline of the Paleolatitude.org 3.0 web interface, and advanced options, including a bulk data option with instructions.

551 and will be made available on the accompanying site www.apwp-online.org [103].
552 Alternatively, the user may select the reference frame based on older APWPs [24, 26, 27].
553 There is also an option for the user to modify the graph axes on the home screen (Figure 4).
554 Finally, the Advanced Options page offers a 'batch option', where the user may
555 upload a data file for bulk paleolatitude computation. There is no maximum number of data,
556 but very large data files (with 10.000s of entries) may take a few hours to compute. The bulk
557 option requires an Excel or CSV file that provides input information on the location, name,
558 and age of the samples, and the desired reference frame (Figure 4).
559

560 7. Comparison with other models

561 We illustrate the use of the new batch option in Paleolatitude.org 3.0 through a comparison
562 with a recently published dataset of tetrapod dinosaurs and their paleogeographic
563 distribution from the Permian to the Cretaceous [199]. This study compiled the data from
564 the global paleobiology database [200]. That database provides a paleolatitude for each of
565 its entries based on reference frames of Scotese and coworkers for older entries [201, 202]
566 or of Wright et al. [203] using a spline-fitted paleomagnetic reference frame of Torsvik and
567 van der Voo [204] for younger entries. However, Heath et al. [199], preferring a more recent
568 plate model and paleomagnetic reference frame, recalculated the paleolatitudes using the
569 GPlates reconstruction of Merdith et al. [19] placed in the paleomagnetic reference frame of
570 Tetley [205].
571 The relative plate motions between the major plates bounded by modern oceans
572 vary little between these different reconstructions, except the China Blocks before the
573 Cretaceous, which vary strongly between models (compare Figure 5e with the rest of the

574 curves). Most differences in predicted paleolatitude arise from the different reference
575 frames used (Figure 5). The Scotese reconstructions use a hybrid of a hotpot reference
576 frame and paleomagnetic reference frame. The reference frame used in Wright et al. [203]
577 corresponds to the 60-550 Ma APWP for Gondwana of Torsvik and van der Voo [204]. This
578 APWP was computed from paleopoles of Gondwanan continents only, using a spherical
579 spline approach in which the paleopoles are weighted based on a set of seven criteria for
580 pole quality (Q-factor [206]). This approach provides a highly smoothed reference frame
581 that does not come with a quantified uncertainty. Because this APWP is not defined for the
582 past 60 Ma, any paleolatitude computed using this APWP is based on an interpolation for
583 almost the entire Cenozoic. This APWP was therefore not intended to serve as a global
584 paleomagnetic reference frame. The same team published updated Gondwanan APWPs, as
585 well as global APWP that also included data from e.g., North America and Eurasia, twice
586 afterward, superseding the original Torsvik and van der Voo work [27, 207].
587 The (unpublished) paleomagnetic reference frame of Tetley [205] uses the paleopole
588 database of Torsvik et al. [27], but 'optimizes' the APWP by an algorithm that aims to
589 minimize both absolute plate velocities as well as their gradients. This algorithm uses an
590 iterative process in which the position and age of each paleopole is allowed to freely change
591 within their errors bounds, until the APWP converges to a path that jointly minimizes the
592 mean APW velocity and velocity gradient. Because this approach does not strictly follow the
593 data, and because the underlying data are averages of poles that in turn are arbitrary
594 collections of data [31], this paleomagnetic reference frame does not come with a
595 geologically meaningful error bar. The version of the paleomagnetic reference frame of
596 Tetley [205] used in the Merdith et al. [19] plate model was constructed using a running
597 mean approach with a 50 Myr time window, leading to enhanced smoothing compared to

598 the Torsvik et al. [27] global APWP for 320-0 Ma. As a result of this approach, polar wander
599 rates were reduced by ~56% compared to pole-averaged running mean paths. However,
600 there is no rationale why polar wander rates must be minimal, and the approach thus
601 smears and averages peaks that may well be signals of paleogeographic change.
602

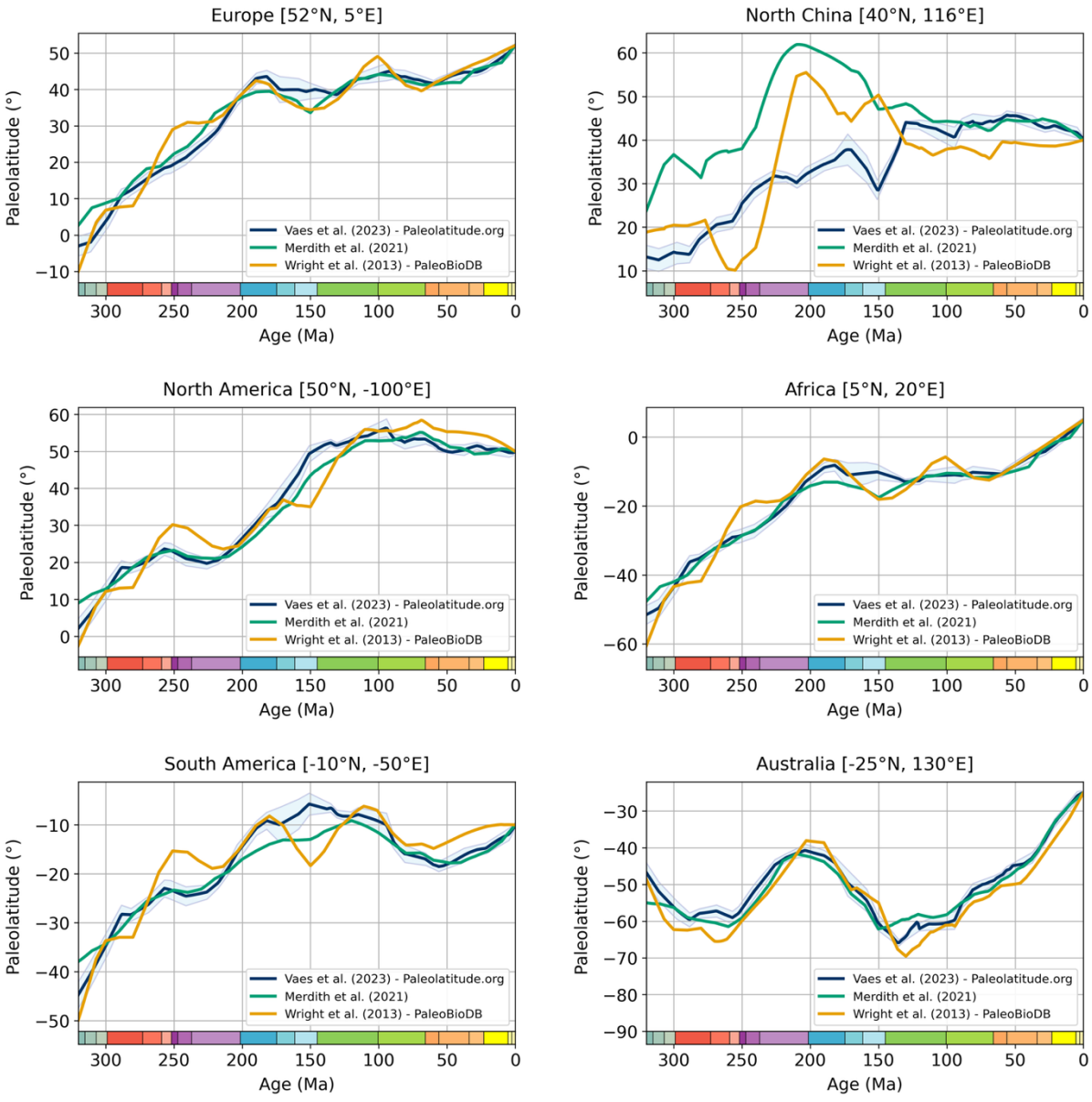

603
604 **Figure 5**. Paleolatitude curves for coordinates in selected major continents illustrating the
605 differences between widely used paleogeographic models.
606

We compare the paleolatitudes computed by Heath et al. [199] based on the Merdith et al. reconstruction with those from Paleolatitude 3.0 (Figure 6a). First, it is clear that the first-order distribution of tetrapod dinosaurs across latitudes that underpinned the interpretations of Heath et al. [199], is robust. However, we may use this dataset to illustrate the differences of the Paleolatitude.org 3.0 model with the other two widely used models. The Merdith et al. and Tetley models [19, 205] give paleolatitudes that are systematically more northerly by up to ~10° between ~270 and 210 Ma, and more southerly by up to ~5° after this time. This difference illustrates the effects of the 50 Myr sliding window and the smoothing optimization approach used by Tetley [205]. In addition, the China blocks in the reconstruction of Merdith et al. [19] are 20-25° farther north than in the Utrecht Paleogeography Model. Differences with the paleolatitudes given in the global paleobiology database are on the same order of magnitude, although these predict latitudes that are systematically more northerly (Figure 6c), by up to 10°.

The differences between these different reconstructions do not change first-order distribution estimates (as illustrated with the Heath et al. [199] dataset, Figure 6), although they may be meaningful for critical intervals such as the paleo-polar circle or paleo-tropics. More importantly, the Paleolatitude.org calculator provides uncertainties that are a function of the error in the paleomagnetic reference frame and the age range assigned to the sample. This opens the opportunity to propagate these uncertainties into quantitative estimates of distributions, for instance in biodiversity gradients, as illustrated below.

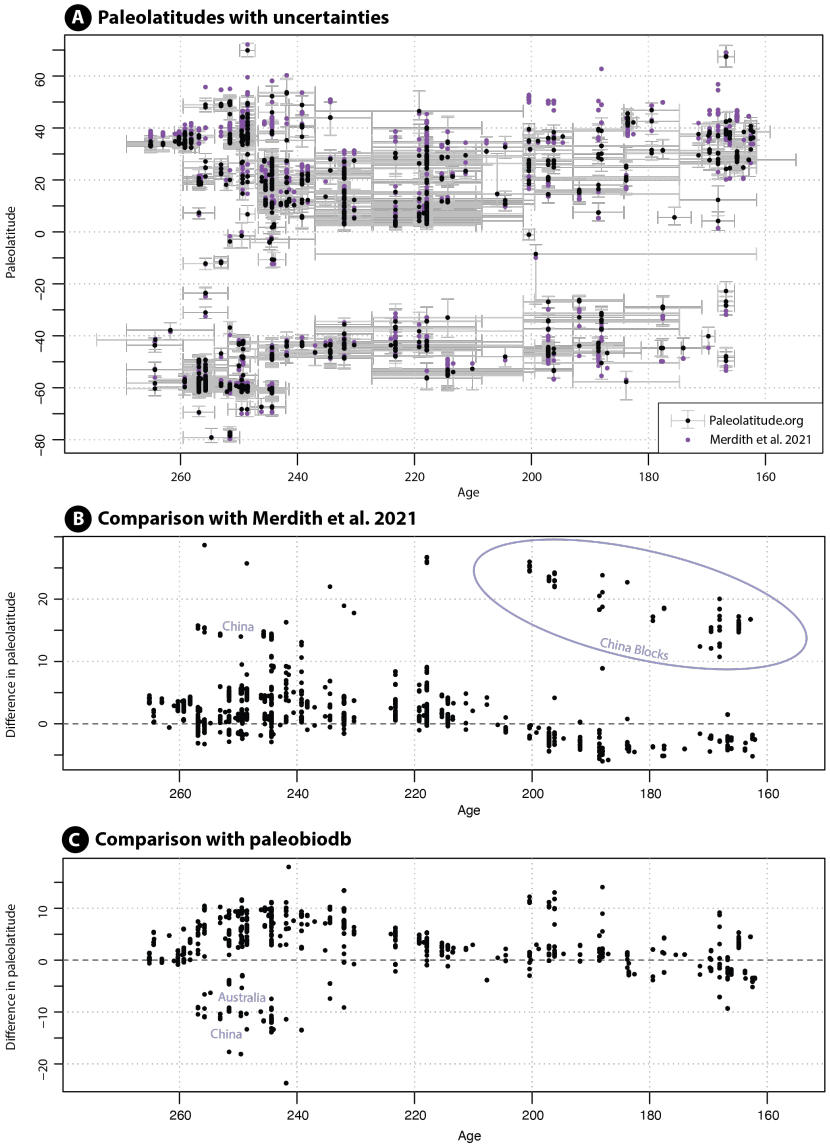

628

629 **Figure. 6**. Differences in paleolatitude estimates for an example dataset of tetrapod
630 dinosaurs found in Upper Permian to Middle Jurassic strata [199]. A) Distribution of data
631 according to the global paleobiology database [200] that uses reference frames of Scotese
632 and coworkers [201, 202] or of Wright et al. [203] using a spline-fitted paleomagnetic
633 reference frame of Torsvik and van der Voo [204]; B) Distribution of data using the
634 reconstruction of Merdith et al. [19] in the unpublished optimized paleomagnetic reference
635 frame of Tetley [205]; C) Data distribution using our new paleogeographic reconstruction in
636 the upgraded gAPWP25 [13]; D) Difference between A and C; E) Difference between B and
637 C.

8. Application: propagating uncertainty in biodiversity gradients

The Latitudinal Diversity Gradient (LDG) is a macroecological pattern of higher taxonomic richness at lower than at at higher latitudes - and more so in marine organisms than in terrestrial ones - that is thought to result from higher and less variable solar irradiance at lower latitudes [208, 209]. The LDG has been sensitive to climatic processes, such as the steepness of the latitudinal temperature gradient or hyperthermal events leading to low-latitude diversity crises [210, 211]. The LDG is computed from fossil occurrence data placed in temporal and paleogeographic context. With the Paleolatitude.org tool, it is now for the first time possible to not only determine for each fossil its paleolatitude at its median age, as has so far been the common approach, but also to include the effects of age and paleolatitudinal uncertainty.

Here we illustrate the use of Paleolatitude.org 3.0 with an example of a collection of ~34,000 Upper Jurassic marine fossils. From these, we calculated the LDG using the Paleobiology Database accessed using the paleobioDB package for R Software [212]. Occurrences for marine fauna identified at least at the genus level were downloaded and uncertain genus identifications were culled. All occurrences whose stratigraphic range overlapped with Late Jurassic and recorded at any spatial resolution were included in our collection. Based on each occurrence's current geographical location and age range, its paleogeographic position was determined with the Paleolatitude.org tool and the paleolatitudinal uncertainty was determined from the combination of the uncertainty in the paleomagnetic reference frame and the age uncertainty of each fossil, as illustrated in Figure 1d. Note that of our dataset, approximately 1000 fossils came from Alaska and the Canadian Cordillera (Figure 7a) that have not been included in our reconstruction yet. We

discarded these data, which would have occupied low- to mid- northern hemisphere paleolatitudes [26, 156]. We stress that the low to mid-latitude LDG in our example is thus likely somewhat underestimated.

The average uncertainty, defined as the difference between the higher and lower bound, for the Upper Jurassic marine genera is 6.8° (Figure 7b), mostly as a function of age uncertainty. We applied no cutoffs or data curation (which may be advisable when carrying out an in-depth LDG study) but used all data for further analysis.

We performed an analysis of Sampled In Bin (SIB) richness gradient and accounted for the uncertainty in paleolatitude using a bootstrap approach. To this end, paleolatitudes were divided into 5° bins. When an occurrence's paleogeographic uncertainty range spanned multiple bins, we calculated the proportion of its latitudinal range falling within each overlapping bin.

In each bootstrap iteration (n = 1000), every occurrence was assigned to one of its overlapping bins, with frequency based on the calculated proportions. For each iteration, we counted the number of unique genera per bin (SIB). The final richness estimate for each bin represents the mean SIB across all iterations, with 95% confidence intervals calculated from the bootstrap distribution (Figure 8). For comparison, we also calculated SIB using point-estimate paleolatitudes only, assigning each occurrence to a single bin based on its estimated paleolatitude without accounting for positional uncertainty (Fig. 8). In most cases, the uncertainty-corrected richness estimates overlap with point-estimates, reflecting the high precision of reconstructed paleolatitudes. Mean SIB richness with uncertainty accounted for is slightly higher than point estimate across the -45° to 45° interval, with the largest difference in the 35°-40° bin, where richness peaks. This is mostly the result of taking age uncertainty into account, which spreads fossils over a wider range of bins than just the

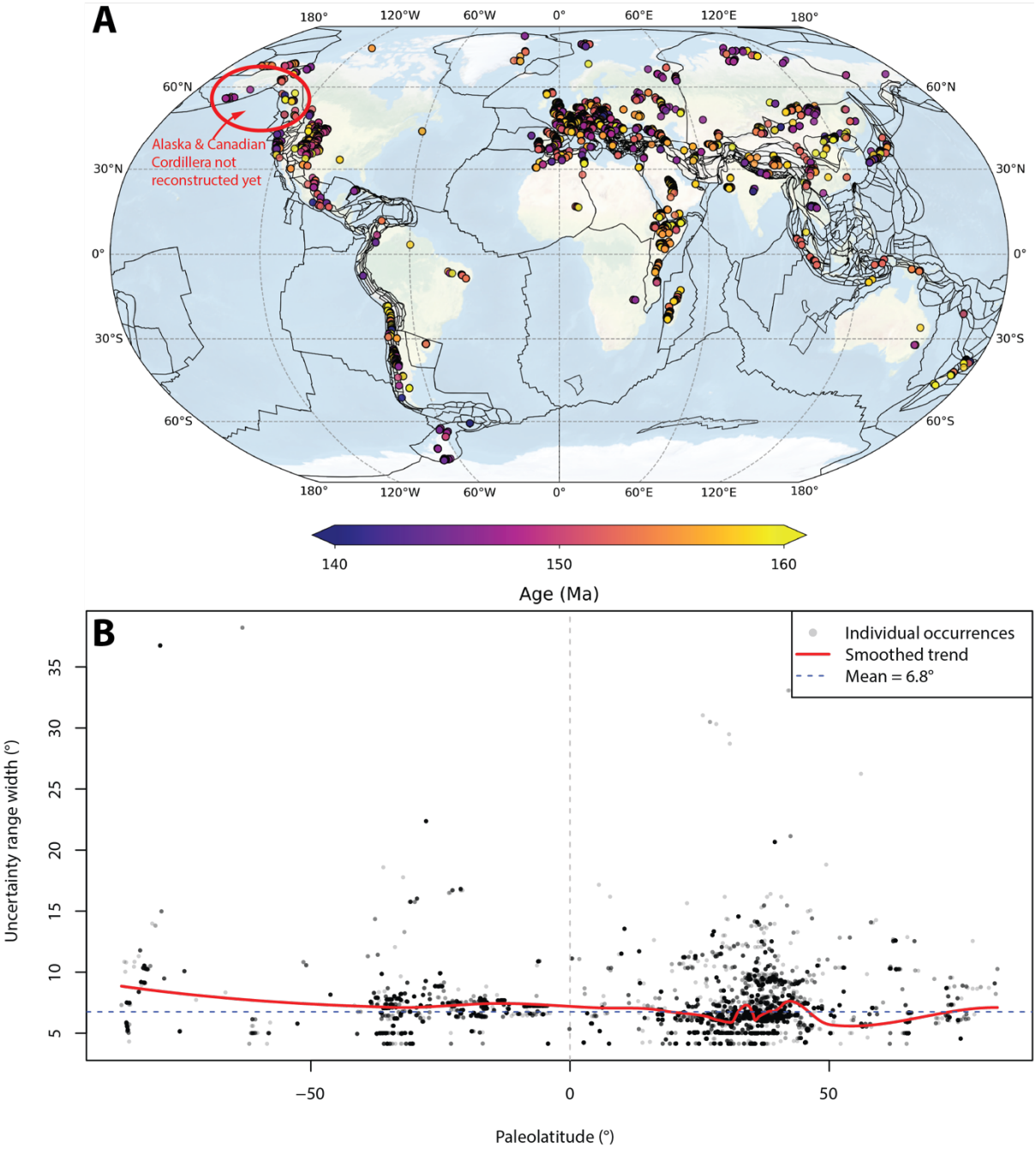

685

686 **Figure 7**. A) Geographic distribution of the marine fossil dataset from the Upper Jurassic
687 used for to compute a Latitudinal Diversity Gradient. B) Paleolatitude precision as a
688 function of paleolatitude. Points indicate individual occurrences, with darker gray
689 indicating more overlying observations. The red line is Loess fit through the data. Based
690 on 33803 observations.

691

692 bin of their median age. Summarizing, our example based on a large dataset of tens of
693 thousands of samples quantitatively corroborates the robustness of LDG calculations in
694 which uncertainties were previously not considered. As illustrated in Figure 8, uncertainties
695 for smaller datasets may be considerably higher and may affect previous conclusions based
696 on the semi-quantitative, error bar-less paleolatitude calculations that have so far been the
697 standard.
698

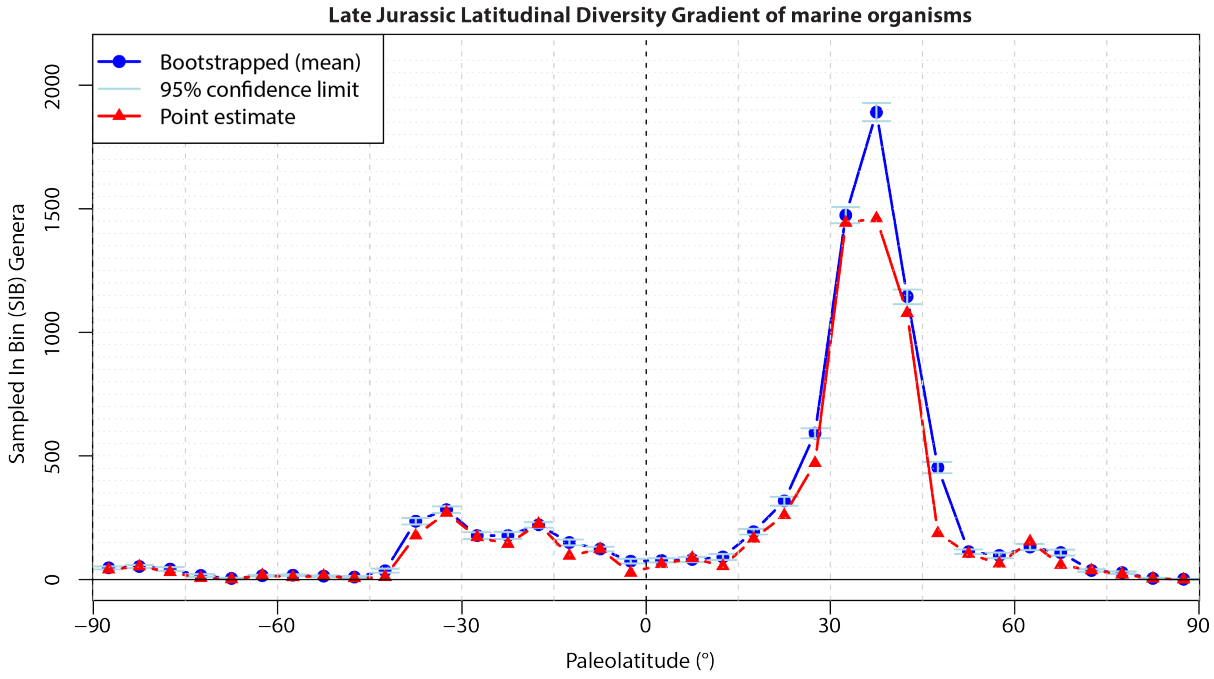

699

700 **Figure 8**. Genus-level Latitudinal Diversity Gradient of marine organisms in the Late Jurassic,
701 without curation, and taking uncertainty in age and the paleomagnetic reference frame into
702 account when computing paleolatitude, reflected in 95% bootstrap confidence intervals.
703 Overlain is a Sampled In Bin point estimate of the LDG in which paleolatitude and age
704 uncertainty is not considered. Based on 33802 occurrences resampled 1000 times into 5°
705 paleolatitude bins (see Supplementary Data).
706

9. Conclusions

In this paper, we provide an upgrade of the Paleolatitude.org webtool to version 3.0. This tool provides estimates of paleolatitude through time for any location on Earth and computes a paleolatitudinal uncertainty that is a function of the underlying paleogeographic reconstruction and the age uncertainty of a sample. The new features include the following:

1) We provide the first global model, back to ~320 Ma, that restores the paleogeographic units that are now thrusted over each other in orogenic (mountain) belts and provide the underlying GPlates reconstruction files. In addition, we provide a brief synopsis of global paleogeography since the Carboniferous, particularly including the formation and demise by collision of microcontinents that existed in the Tethyan, and to a lesser extent, the Panthalassa/Paleo-Pacific Oceans.

2) We place this reconstruction into a recent, more precise paleomagnetic reference frame that is based on site-level paleomagnetic data. In this paper, we provide the first update of its underlying database, increasing the database by ~10% and further decreasing uncertainty.

3) We introduce a new online interface with an easy-to-use tool with a batch option that allows computing paleolatitudinal data for essentially unlimited datasets.

4) Finally, we illustrate differences with previous reconstructions and explain these differences. We show an application by calculating a paleolatitudinal biodiversity gradient for the late Jurassic in which we use a bootstrap approach to propagate paleolatitude and age uncertainty into the result.

Acknowledgements

DJJvH, BV, SHAvdL, and NL acknowledge NWO Vici grant 865.17.001 to DJJvH. LMB acknowledges NWO Veni grant 212.247. BV acknowledges support from the ERC consolidator grants to Pietro Sternai (MATRICs, grant No. 101167761) and to Alexis Licht (DISPERSAL, grant No. 101043268). EJ was supported by an ERC starting grant (MindTheGap, grant No. 101041077). M. Carrano, M. Clapham, T. Danelian, H. Eichiner, F. Fürsich, M. Gahr, D. Hempfling, A. Hendy, S. Hicks, W. Kiessling, A. Kocsis, K. Layou, E. Link, J. Martinelli, U. Merkel, S. Nürnberg, W. Puijk, P. Schossleitner, L. Villier contributed the largest part of fossil occurrences to the database used in this study.

Data Availability Statement

Code and data used in LDG analysis of Figure 8 is available at DOI:

https://doi.org/10.5281/zenodo.18183857

Author contributions

D.J.J.v.H. designed the research. D.J.J.v.H., B.V., L.M.B., N.L., S.H.A.v.d.L., E.L.A., S.d.B. made the global paleogeographic reconstruction. B.V., D.J.J.v.H. compiled paleomagnetic data. B.V. analyzed paleomagnetic data and computed gAPWP25. B.V., M.F., J.P. updated and added to the code of the web tools. J.P. built the Paleomagnetism.org 3.0 website. D.J.J.v.H., B.V., E.J. wrote the manuscript. D.J.J.v.H., B.V., L.M.B., E.J. drafted figures. All authors read and edited the manuscript.

Supplementary Information

Supplementary Files: A set of supplementary files is available at DOI: https://doi.org/10.6084/m9.figshare.31021144, containing the following elements:

Supplementary Files 1: GPlates files (www.gplates.org [14]) of the Utrecht Paleogeography Model presented in the paleogeographic maps of Figures 1 and 3, and the rigid polygon version that is used as basis for the Paleolatitude.org tool. These consist of a rotation file, and a series of shape files (in gpml format) that underpin the paleogeographic model, a gpml file of the rigid polygons that are used to rotate coordinates in the Paleolatitude.org tool, as well as a project file (gproj) of the entire paleogeographic reconstruction.

Supplementary Files 2: Details of gAPWP25. In addition to a Readme.txt file with general descriptions and the gAPWP25.rot file with the updated paleomagnetic reference frame in GPlates rotation format, the files contain:

Table S1: Changelog of the update of gAPWP23 to gAPWP25

Table S2: Paleomagnetic database used to compute the global apparent polar wander path for the last 320 Ma. We have listed age constraints, statistical parameters, Euler rotation parameters and other metadata per paleomagnetic pole used in the parametric re-sampling scheme. For more details, see main text. The grey-colored entries are excluded from the computation of the APWP. See columns 'age constraints', 'comments' and 'reliability' for specific details for a given dataset. Abbreviations: min_age and max_age = lower and upper boundaries of age uncertainty range; slat/slon = latitude and longitude of (mean) sampling location; N = number of paleomagnetic sites used to compute the paleopole; mDec/mInc =

mean declination of inclination; α95/A95 = radius of the 95% confidence circle about the mean of the distribution of directions/VGPs; k/K = Fisher [109] precision parameter of the distribution of directions/VGPs; plat/plon = paleopole latitude and longitude (south pole); K_est/A95_est = values estimated using formula of Cox [213] (eq. 24); plateID = plate identification number; Rlat/Rlon = paleopole latitude and longitude in coordinate frame of South Africa; EP_lat/EP_lon/EP_ang = total reconstruction pole parameters for rotating the paleopole to South Africa coordinates; f = flattening factor (only for sedimentary data), p_std = standard deviation of the assumed normal distributed co-latitudes, obtained from E/I correction (only for sedimentary data); Deenen = indicates whether the N-dependent reliability envelope of Deenen et al. [214] is satisfied (TRUE or FALSE) or, in case of sediment-derived datasets, the quality grade (A, B or C) following the evaluation scheme of Vaes et al. [106]; excl = reason for exclusion (R = rejected because entry is a duplicate, N < 5, age range > 20 Ma, remagnetized or otherwise considered unreliable, see comments/reliability column); refno = reference number in global paleomagnetic database [215, 216]; DB = database in which entry is listed (T12 [27], PSV10 [217], gAPWP23 [13], gAPWP25 = added in this study).

Table S3: Global plate circuit used to transfer paleomagnetic data to a single reference plate, from Vaes et al. [13] with minor modification in the rotation parameters for India. See Vaes et al. [13] for references and details.

Table S4: gAPWP25 rotated in the coordinates of the major continents.

Supplementary Files 3

Table S5: Euler rotations of every polygon relative to South Africa (701) at times corresponding to the ages of the reference poles of gAPWP25, using the rotation file of the

799 Utrecht Paleogeography Model in Supplementary Files 1. Paleolatitudes provided by

800 Paleolatitude.org 3.0 are interpolated from these rotations.

9. References

1. Goldreich P, Toomre A. Some remarks on polar wandering. Journal of Geophysical Research. 1969;74(10):2555-67. doi: 10.1029/JB074i010p02555.
2. Cocks LRM, Torsvik TH. Ordovician palaeogeography and climate change. Gondwana Research. 2021;100:53-72.
3. van der Meer DG, Scotese CR, Mills BJ, Sluijs A, van de Weg RM. Long-term Phanerozoic global mean sea level: Insights from strontium isotope variations and estimates of continental glaciation. Gondwana Research. 2022.
4. Scotese CR, Song H, Mills BJ, van der Meer DG. Phanerozoic paleotemperatures: The earth's changing climate during the last 540 million years. Earth-Science Reviews. 2021;215:103503.
5. Müller RD, Zahirovic S, Williams SE, Cannon J, Seton M, Bower DJ, et al. A global plate model including lithospheric deformation along major rifts and orogens since the Triassic. Tectonics. 2019.
6. van Hinsbergen DJJ, de Groot LV, van Schaik SJ, Spakman W, Bijl PK, Sluijs A, et al. A Paleolatitude Calculator for Paleoclimate Studies. PLoS One. 2015;10(6):e0126946. Epub 2015/06/11. doi: 10.1371/journal.pone.0126946. PubMed PMID: 26061262; PubMed Central PMCID: PMCPMC4462584.
7. Judd EJ, Tierney JE, Huber BT, Wing SL, Lunt DJ, Ford HL, et al. The PhanSST global database of Phanerozoic sea surface temperature proxy data. Scientific data. 2022;9(1):1-38.
8. Bijl PK. DINOSTRAT: a global database of the stratigraphic and paleolatitudinal distribution of Mesozoic–Cenozoic organic-walled dinoflagellate cysts. Earth System Science Data. 2022;14(2):579-617.
9. Auderset A, Moretti S, Taphorn B, Ebner P-R, Kast E, Wang XT, et al. Enhanced ocean oxygenation during Cenozoic warm periods. Nature. 2022;609(7925):77-82.
10. O'Brien CL, Robinson SA, Pancost RD, Damsté JSS, Schouten S, Lunt DJ, et al. Cretaceous sea-surface temperature evolution: Constraints from TEX86 and planktonic foraminiferal oxygen isotopes. Earth-Science Reviews. 2017;172:224-47.
11. Leprieur F, Descombes P, Gaboriau T, Cowman PF, Parravicini V, Kulbicki M, et al. Plate tectonics drive tropical reef biodiversity dynamics. Nature Communications. 2016;7(1):1-8.
12. Gradstein FM, Ogg JG, Schmitz MD, Ogg GM. Geologic time scale 2020: Elsevier; 2020.
13. Vaes B, van Hinsbergen DJJ, van de Lagemaat SHA, van der Wiel E, Lom N, Advokaat E, et al. A global apparent polar wander path for the last 320 Ma calculated from site-level paleomagnetic data. Earth-Science Reviews. 2023;245:104547. doi: https://doi.org/10.31223/X55368.
14. Müller RD, Cannon J, Qin X, Watson RJ, Gurnis M, Williams S, et al. GPlates: building a virtual Earth through deep time. Geochemistry, Geophysics, Geosystems. 2018;19(7):2243-61.
15. Butler RF. Paleomagnetism: magnetic domains to geologic terranes: Blackwell Scientific Publications Boston; 1992.
16. Tauxe L. Essentials of paleomagnetism: Univ of California Press; 2010.

17. Buffan L, Jones LA, Domeier M, Scotese CR, Zahirovic S, Varela S. Mind the uncertainty: Global plate model choice impacts deep-time palaeobiological studies. Methods in Ecology and Evolution. 2023;14(12):3007-19.
18. Torsvik TH, Cocks LRM. Earth history and palaeogeography: Cambridge University Press; 2017.
19. Merdith AS, Williams SE, Collins AS, Tetley MG, Mulder JA, Blades ML, et al. Extending full-plate tectonic models into deep time: Linking the neoproterozoic and the phanerozoic. Earth-Science Reviews. 2021;214:103477.
20. Scotese CR. An Atlas of Phanerozoic Paleogeographic Maps: The Seas Come In and the Seas Go Out. Annual Review of Earth and Planetary Sciences. 2021;49.
21. Cox A, Hart RB. Plate tectonics: how it works: John Wiley & Sons; 1986.
22. Doubrovine PV, Tarduno JA. Linking the Late Cretaceous to Paleogene Pacific plate and the Atlantic bordering continents using plate circuits and paleomagnetic data. Journal of Geophysical Research. 2008;113(B7). doi: 10.1029/2008jb005584.
23. Seton M, Müller RD, Zahirovic S, Gaina C, Torsvik T, Shephard G, et al. Global continental and ocean basin reconstructions since 200Ma. Earth-Science Reviews. 2012;113(3-4):212-70. doi: 10.1016/j.earscirev.2012.03.002.
24. Besse J, Courtillot V. Apparent and true polar wander and the geometry of the geomagnetic field over the last 200 Myr. Journal of Geophysical Research: Solid Earth. 2002;107(B11):EPM 6-1-EPM 6-31. doi: 10.1029/2000jb000050.
25. Besse J, Courtillot V. Revised and synthetic apparent polar wander paths of the African, Eurasian, North American and Indian Plates, and true polar wander since 200 Ma. Journal of Geophysical Research: Solid Earth. 1991;96(B3):4029-50. doi: 10.1029/90jb01916.
26. Kent DV, Irving E. Influence of inclination error in sedimentary rocks on the Triassic and Jurassic apparent pole wander path for North America and implications for Cordilleran tectonics. Journal of Geophysical Research. 2010;115(B10). doi: 10.1029/2009jb007205.
27. Torsvik TH, Van der Voo R, Preeden U, Mac Niocaill C, Steinberger B, Doubrovine PV, et al. Phanerozoic polar wander, palaeogeography and dynamics. Earth-Science Reviews. 2012;114(3-4):325-68. doi: 10.1016/j.earscirev.2012.06.007.
28. Torsvik TH, Müller RD, Van der Voo R, Steinberger B, Gaina C. Global plate motion frames: Toward a unified model. Reviews of Geophysics. 2008;46(3). doi: 10.1029/2007rg000227.
29. van Hinsbergen DJJ, van Schaik SJ. Paleolatitude. org 2.0: The paleolatitude calculator extended back to 550 Ma (online comment). PLoS One. 2016:https://tinyurl.com/323wr5ns.
30. Rowley DB. Comparing Paleomagnetic Study Means with Apparent Wander Paths: A Case Study and Paleomagnetic Test of the Greater India versus Greater Indian Basin Hypotheses. Tectonics. 2019;38:722-40.
31. Vaes B, Gallo LC, van Hinsbergen DJJ. On pole position: causes of dispersion of the paleomagnetic poles behind apparent polar wander paths. Journal of Geophysical Research. 2022:e2022JB023953. doi: 10.1029/2022JB023953.
32. Wilson DS, DeMets C. Changes in motion of the Nazca/Farallon plate over the last 34 million years: Implications for flat-slab subduction and the propagation of plate kinematic changes. Journal of Geophysical Research: Solid Earth. 2025;130(11):e2025JB031933.
33. DeMets C, Merkouriev S. Detailed reconstructions of India–Somalia Plate motion, 60 Ma to present: implications for Somalia Plate absolute motion and India–Eurasia Plate motion. Geophysical Journal International. 2021;227(3):1730-67.

34. DeMets C, Merkouriev S. High-resolution reconstructions of South America plate motion relative to Africa, Antarctica and North America: 34 Ma to present. Geophysical Journal International. 2019;217(3):1821-53.
35. DeMets C, Merkouriev S. High-resolution estimates of Nubia–Somalia plate motion since 20 Ma from reconstructions of the Southwest Indian Ridge, Red Sea and Gulf of Aden. Geophysical Journal International. 2016;207(1):317-32.
36. Gürer D, Granot R, van Hinsbergen DJJ. Plate tectonic chain reaction revealed by noise in the Cretaceous Quiet Zone. Nature Geoscience. 2022;15:233-9. doi: https://doi.org/10.31223/X5J626.
37. Shephard GE, Abdelmalak MM, Faleide JI, Clennett E, Zahirovic S, Gac S, et al. Multi-phase intra-plate rifting and deformable plate modelling of the Northeast Atlantic back to the Permian. Gondwana Research. 2025;149:465-90.
38. King MT, Welford JK, Cadenas P, Tugend J. Investigating the plate kinematics of the Bay of Biscay using deformable plate tectonic models. Tectonics. 2021;40(7):e2020TC006467.
39. Welford JK, Brune S, Neuharth D, King MT. Ancient scars and rotating ribbons: Appalachian–Caledonian orogenic influence on the genesis of the Flemish Cap and the Porcupine Bank during Mesozoic North Atlantic rifting. Geological Society, London, Special Publications. 2025;557(1):SP557-2023-212.
40. King MT, Welford JK. Advances in deformable plate tectonic models: 2. Reconstructing the southern North Atlantic back through time. Geochemistry, Geophysics, Geosystems. 2022;23(6):e2022GC010373.
41. van Hinsbergen DJJ, Schouten TLA. Deciphering paleogeography from orogenic architecture: constructing orogens in a future supercontinent as thought experiment. American Journal of Science. 2021;321:955-1031. doi: DOI 10.2475/06.2021.09.
42. van Hinsbergen DJJ, Kapp P, Dupont-Nivet G, Lippert PC, DeCelles PG, Torsvik TH. Restoration of Cenozoic deformation in Asia and the size of Greater India. Tectonics. 2011;30(5):n/a-n/a. doi: 10.1029/2011tc002908.
43. Eichelberger N, McQuarrie N. Kinematic reconstruction of the Bolivian orocline. Geosphere. 2015;11(2):445-62.
44. Schepers G, van Hinsbergen DJJ, Spakman W, Kosters ME, Boschman LM, McQuarrie N. South-American plate advance and forced Andean trench retreat as drivers for transient flat subduction episodes. Nat Commun. 2017;8:15249. Epub 2017/05/17. doi: 10.1038/ncomms15249. PubMed PMID: 28508893; PubMed Central PMCID: PMCPMC5440808.
45. Teixell A, Arboleya M-L, Julivert M, Charroud M. Tectonic shortening and topography in the central High Atlas (Morocco). Tectonics. 2003;22(5):n/a-n/a. doi: 10.1029/2002tc001460.
46. Jolivet L, Brun J-P. Cenozoic geodynamic evolution of the Aegean. International Journal of Earth Sciences. 2010;99(1):109-38.
47. McQuarrie N, Wernicke BP. An animated tectonic reconstruction of southwestern North America since 36 Ma. Geosphere. 2005;1:147-72. doi: 10.1130/ges00016.1.
48. Van Horne A, Sato H, Ishiyama T. Evolution of the Sea of Japan back-arc and some unsolved issues. Tectonophysics. 2017;710:6-20.
49. van Hinsbergen DJJ, Schmid SM. Map view restoration of Aegean-West Anatolian accretion and extension since the Eocene. Tectonics. 2012;31(5):doi: 10.1029/2012tc003132. doi: 10.1029/2012tc003132.

50. Boschman LM, van Hinsbergen DJJ, Torsvik TH, Spakman W, Pindell JL. Kinematic reconstruction of the Caribbean region since the Early Jurassic. Earth-Science Reviews. 2014;138:102-36. doi: 10.1016/j.earscirev.2014.08.007.
51. van Hinsbergen DJJ, Torsvik T, Schmid SM, Matenco L, Maffione M, Vissers RLM, et al. Orogenic architecture of the Mediterranean region and kinematic reconstruction of its tectonic evolution since the Triassic. Gondwana Research. 2020;81:79-229.
52. Philippon M, Cornée J-J, Münch P, van Hinsbergen DJJ, BouDagher-Fadel M, Gailler L, et al. Eocene intra-plate shortening responsible for the rise of a faunal pathway in the northeastern Caribbean realm. PloS one. 2020;15(10):e0241000.
53. Dalziel IWD, Lawver LA, Norton IO, Gahagan LM. The Scotia Arc: Genesis, Evolution, Global Significance. Annual Review of Earth and Planetary Sciences. 2013;41(1):767-93. doi: 10.1146/annurev-earth-050212-124155.
54. Eagles G, Livermore R, Morris P. Small basins in the Scotia Sea: The Eocene Drake Passage gateway. Earth and Planetary Science Letters. 2006;242(3-4):343-53. doi: 10.1016/j.epsl.2005.11.060.
55. Garrocq C, Lallemand S, Marcaillou B, Lebrun Jf, Padron C, Klingelhoefer F, et al. Genetic relations between the Aves Ridge and the Grenada back-arc Basin, East Caribbean Sea. Journal of Geophysical Research: Solid Earth. 2021;126(2):e2020JB020466.
56. Sdrolias M, Roest WR, Müller RD. An expression of Philippine Sea plate rotation: the Parece Vela and Shikoku Basins. Tectonophysics. 2004;394(1-2):69-86. doi: 10.1016/j.tecto.2004.07.061.
57. Montheil L, Philippon M, Münch P, Camps P, Vaes B, Cornée Jj, et al. Paleomagnetic rotations in the northeastern Caribbean region reveal major intraplate deformation since the Eocene. Tectonics. 2023;42:e2022TC007706.
58. Dilek Y, Furnes H. Ophiolite genesis and global tectonics: Geochemical and tectonic fingerprinting of ancient oceanic lithosphere. Geological Society of America Bulletin. 2011;123(3-4):387-411. doi: 10.1130/b30446.1.
59. Dewey JF. Ophiolite obduction. Tectonophysics. 1976;31:93-120.
60. Searle MP, Cox JON. Subduction zone metamorphism during formation and emplacement of the Semail ophiolite in the Oman Mountains. Geological Magazine. 2002;139(03). doi: 10.1017/s0016756802006532.
61. Robertson AHF. Overview of the genesis and emplacement of Mesozoic ophiolites in the Eastern Mediterranean Tethyan region. Lithos. 2002;65(1-2):1-67.
62. Maffione M, van Hinsbergen DJJ. Reconstructing plate boundaries in the Jurassic Neo-Tethys from the East and West Vardar Ophiolites (Greece, Serbia). Tectonics. 2018. doi: 10.1002/2017tc004790.
63. Maffione M, van Hinsbergen DJJ, de Gelder GINO, van der Goes FC, Morris A. Kinematics of Late Cretaceous subduction initiation in the Neo-Tethys Ocean reconstructed from ophiolites of Turkey, Cyprus, and Syria. Journal of Geophysical Research: Solid Earth. 2017;122(5):3953-76. doi: 10.1002/2016jb013821.
64. Yumul Jr GP, Dimalanta CB, Tamayo Jr RA, Maury RC. Collision, subduction and accretion events in the Philippines: a synthesis. Island Arc. 2003;12(2):77-91.
65. Whattam SA. Arc-continent collisional orogenesis in the SW Pacific and the nature, source and correlation of emplaced ophiolitic nappe components. Lithos. 2009;113(1-2):88-114. doi: 10.1016/j.lithos.2008.11.009.

66. Iturralde-Vinent M, García-Casco A, Rojas-Agramonte Y, Proenza Fernández JA, Murphy J, Stern R. The geology of Cuba: A brief overview and synthesis. GSA Today. 2016;26:4-10.
67. Wakabayashi J. Upper-plate versus lower-plate ophiolitic assemblages and their significance in interpreting orogenic belt evolution and processes. In: Riggs N, Putirka K, Wakabayashi J, editors. The Virtue of Fieldwork in Volcanology, Sedimentology, Structural Geology, and Tectonics—Celebrating the Career of Cathy Busby: Geological Society of America Special Papers; 2025.
68. Schmid SM, Bernoulli D, Fügenschuh B, Georgiev N, Kounov A, Matenco L, et al. Tectonic units of the Alpine collision zone between Eastern Alps and Western Turkey. Gondwana Research. 2020;78:308-74.
69. Teixell A, Labaume P, Ayarza P, Espurt N, de Saint Blanquat M, Lagabrielle Y. Crustal structure and evolution of the Pyrenean-Cantabrian belt: A review and new interpretations from recent concepts and data. Tectonophysics. 2018;724:146-70.
70. van Hinsbergen DJJ, Gürer D, Koç A, Lom N. Shortening and extrusion in the East Anatolian Plateau: How was Neogene Arabia-Eurasia convergence tectonically accommodated? Earth and Planetary Science Letters. 2024;641:118827.
71. Handy MR, Schmid SM, Bousquet R, Kissling E, Bernoulli D. Reconciling plate-tectonic reconstructions of Alpine Tethys with the geological–geophysical record of spreading and subduction in the Alps. Earth-Science Reviews. 2010;102(3-4):121-58.
72. McQuarrie N. Crustal scale geometry of the Zagros fold–thrust belt, Iran. Journal of Structural Geology. 2004;26(3):519-35. doi: 10.1016/j.jsg.2003.08.009.
73. Yin A. Cenozoic tectonic evolution of the Himalayan orogen as constrained by along-strike variation of structural geometry, exhumation history, and foreland sedimentation. Earth-Science Reviews. 2006;76(1-2):1-131. doi: 10.1016/j.earscirev.2005.05.004.
74. Wakita K. Cretaceous accretionary–collision complexes in central Indonesia. Journal of Asian Earth Sciences. 2000;18(6):739-49.
75. Advokaat EL, van Hinsbergen DJJ. Finding Argoland: reconstructing a microcontinental archipelago from the SE Asian accretionary orogen. Gondwana Research. 2024;128:161-263.
76. Hall R. The Eurasian SE Asian margin as a modern example of an accretionary orogen. Geological Society, London, Special Publications. 2009;318(1):351-72. doi: 10.1144/sp318.13.
77. Isozaki Y, Aoki K, Nakama T, Yanai S. New insight into a subduction-related orogen: A reappraisal of the geotectonic framework and evolution of the Japanese Islands. Gondwana Research. 2010;18(1):82-105. doi: 10.1016/j.gr.2010.02.015.
78. Mortimer N. New Zealand's Geological Foundations. Gondwana Research. 2004;7(1):261-72. doi: 10.1016/s1342-937x(05)70324-5.
79. Plafker G, Nokleberg WJ, Lull J. Bedrock geology and tectonic evolution of the Wrangellia, Peninsular, and Chugach terranes along the Trans-Alaska Crustal Transect in the Chugach Mountains and southern Copper River Basin, Alaska. Journal of Geophysical Research: Solid Earth. 1989;94(B4):4255-95.
80. Isozaki Y, Maruyama S, Furuoka F. Accreted oceanic materials in Japan. Tectonophysics. 1990;181(1-4):179-205.
81. Wakabayashi J, Orme DA. The classic forearc triad of the Franciscan subduction complex, Coast Range ophiolite, and Great Valley forearc basin, eastern California Coast Ranges. 2025.

82. Maremmani A, van Hinsbergen DJ, Advokaat EL, Kotowski AJ, Guilmette C. Orogenic architecture diagrams to reconstruct paleogeography and plate tectonics: Newfoundland (Canada) as a case study. Journal of the Geological Society of London. 2025;submitted, preprint at https://doi.org/10.31223/X5GM80.
83. van de Lagemaat SH, Swart ML, Vaes B, Kosters ME, Boschman LM, Burton-Johnson A, et al. Subduction initiation in the Scotia Sea region and opening of the Drake Passage: When and why? Earth-Science Reviews. 2021:103551.
84. Montheil L, van Hinsbergen DJ, Philippon M, Boschman LM, Cornée J-J, Audemard F, et al. Caribbean biodiversity shaped by subduction zone processes along the Lesser Antilles arch. Communications Earth & Environment. 2025;6(1):900.
85. Arkula C, Lom N, Wakabayashi J, Rea-Downing G, Qayyum A, Dekkers MJ, et al. The forearc ophiolites of California formed during trench-parallel spreading: Kinematic reconstruction of the western USA Cordillera since the Jurassic. Earth-Science Reviews. 2023;237:104275.
86. van Hinsbergen DJJ, Vissers RLM, Spakman W. Origin and consequences of western Mediterranean subduction, rollback, and slab segmentation. Tectonics. 2014;33(4):393-419.
87. van Hinsbergen DJ, Granot R, Vaes B, Vissers RLM. Tectonic mode switches in the Pyrenees caused by Africa-Eurasia rotation pole drift. Nature Geoscience. 2026;submitted; preprint at https://doi.org/10.21203/rs.3.rs-8017726/v1.
88. Lom N, van Hinsbergen DJJ. Reconstruction of plate tectonic evolution and orogenesis of the Central Tethysides (Iran, Afghanistan) since the Permian. Gondwana Research. 2026;submitted, preprint at https://doi.org/10.31223/X5N760.
89. McQuarrie N, van Hinsbergen DJJ. Retrodeforming the Arabia-Eurasia collision zone: Age of collision versus magnitude of continental subduction. Geology. 2013;41(3):315-8. doi: 10.1130/g33591.1.
90. van Hinsbergen DJJ, Maffione M, Koornneef LMT, Guilmette C. Kinematic and paleomagnetic restoration of the Semail ophiolite (Oman) reveals subduction initiation along an ancient Neotethyan fracture zone. Earth and Planetary Science Letters. 2019;518:183-96.
91. van Hinsbergen DJJ, Lippert PC, Li S, Huang W, Advokaat EL, Spakman W. Reconstructing Greater India: Paleogeographic, kinematic, and geodynamic perspectives. Tectonophysics. 2019;760:69-94. doi: 10.1016/j.tecto.2018.04.006.
92. van Hinsbergen DJJ, Lippert PC, Dupont-Nivet G, McQuarrie N, Doubrovine PV, Spakman W, et al. Greater India Basin hypothesis and a two-stage Cenozoic collision between India and Asia. Proc Natl Acad Sci U S A. 2012;109(20):7659-64. doi: 10.1073/pnas.1117262109. PubMed PMID: 22547792; PubMed Central PMCID: PMCPMC3356651.
93. van de Lagemaat SHA, van Hinsbergen DJJ. Plate tectonic cross-roads: Reconstructing the Panthalassa-Neotethys Junction Region from Philippine Sea Plate and Australasian oceans and orogens. Gondwana Research. 2024;126:129-201. doi: https://doi.org/10.1016/j.gr.2023.09.013.
94. van de Lagemaat SH, van Hinsbergen DJJ, Boschman LM, Kamp PJ, Spakman W. Southwest Pacific absolute plate kinematic reconstruction reveals major Cenozoic Tonga-Kermadec slab dragging. Tectonics. 2018;37(8):2647-74.
95. Vaes B, van Hinsbergen DJJ, Boschman LM. Reconstruction of subduction and back-arc spreading in the NW Pacific and Aleutian Basin: Clues to causes of Cretaceous and Eocene plate reorganizations. Tectonics. 2019;38(4):1367-413.

96. Boschman LM, van Hinsbergen DJJ, Spakman W. Reconstructing Jurassic-Cretaceous intra-oceanic subduction evolution in the northwestern Panthalassa Ocean using Ocean Plate Stratigraphy from Hokkaido, Japan. Tectonics. 2021;40:e2019TC005673.
97. Li Z, Ding L, van Hinsbergen DJJ, Lippert PC, Yue Y, Xie J, et al. Jurassic true polar wander recorded by the Lhasa terrane on its northward journey from Gondwana to Eurasia. Earth and Planetary Science Letters. 2022;592:117609.
98. Wang T, Zhou Y, van Hinsbergen DJ, Sun J, Cheng X, Chai R, et al. Paleomagnetic Evidence for a Late Permian Qaidam-North China Connection, and the Cryptic Final Mesozoic Intra-Asian Suture. Journal of Geophysical Research: Solid Earth. 2025;130(8):e2025JB031123.
99. Song P, Ding L, Li Z, Lippert PC, Yue Y. An early bird from Gondwana: Paleomagnetism of Lower Permian lavas from northern Qiangtang (Tibet) and the geography of the Paleo-Tethys. Earth and Planetary Science Letters. 2017;475:119-33. doi: 10.1016/j.epsl.2017.07.023.
100. Van der Voo R, van Hinsbergen DJJ, Domeier M, Spakman W, Torsvik TH. Latest Jurassic–earliest Cretaceous closure of the Mongol-Okhotsk Ocean: A paleomagnetic and seismological-tomographic analysis. Late Jurassic Margin of Laurasia–A Record of Faulting Accommodating Plate Rotation. Geological Society of America Special Papers2015. p. 589-606.
101. Koymans MR, van Hinsbergen DJJ, Pastor-Galan D, Vaes B, Langereis CG. Towards FAIR paleomagnetic data management through Paleomagnetism. org 2.0. Geochemistry, Geophysics, Geosystems. 2020:e2019GC008838.
102. Koymans MR, Langereis CG, Pastor-Galán D, van Hinsbergen DJJ. Paleomagnetism.org: An online multi-platform open source environment for paleomagnetic data analysis. Computers & Geosciences. 2016;93:127-37. doi: 10.1016/j.cageo.2016.05.007.
103. Vaes B, van Hinsbergen DJ, Paridaens J. APWP-online. org: a global reference database and open-source tools for calculating apparent polar wander paths and relative paleomagnetic displacements. Tektonika. 2024;2:173-88.
104. Gallo LC, Domeier M, Sapienza F, Swanson-Hysell NL, Vaes B, Zhang Y, et al. Embracing uncertainty to resolve polar wander: A case study of Cenozoic North America. Geophysical Research Letters. 2023;50(11):e2023GL103436.
105. Mirzaei M, Burmester RF, Housen BA, Kravchinsky VA. Paleomagnetic consequence of thermal evolution of the North American Passive Margin: The Jurassic APWP controversy. Gondwana Research. 2025;140:89-100.
106. Vaes B, Li S, Langereis CG, van Hinsbergen DJJ. Reliability of palaeomagnetic poles from sedimentary rocks. Geophysical Journal International. 2021;225:1281–303.
107. Heslop D, Scealy JL, Wood AT, Tauxe L, Roberts AP. A bootstrap common mean direction test. Journal of Geophysical Research: Solid Earth. 2023;128(8):e2023JB026983.
108. Tauxe L, Heslop D, Gilder SA. Assessing paleosecular variation averaging and correcting paleomagnetic inclination shallowing. Journal of Geophysical Research: Solid Earth. 2024;129(8):e2024JB029502.
109. Fisher R. Dispersion on a sphere. Proceedings of the Royal Society of London Series A Mathematical and Physical Sciences. 1953;217(1130):295-305.
110. Tauxe L, Kent DV. A simplified statistical model for the geomagnetic field and the detection of shallow bias in paleomagnetic inclinations: was the ancient magnetic field dipolar? 2004.

111. Doll P, Turner GM, Kennedy BM, Nichols AR, Greve A, Cole JW, et al. Paleomagnetism-based chronology of Holocene lava flows at Mt Ruapehu, Aotearoa New Zealand. Geochemistry, Geophysics, Geosystems. 2024;25(9):e2024GC011745.
112. Sebastián-Reyes JD, García-Ruiz R, Avellán D-R, Goguitchaichvili A, Ruiz RC, Kravchinsky V, et al. Paleomagnetic study of Tres Vírgenes Volcanic Complex, Baja California, Mexico. Journal of South American Earth Sciences. 2025;151:105238.
113. Pasqualon N, Savian J, Lima E, de Oliveira W, Hartmann G, Scherer C, et al. New volcanological, 40Ar/39Ar dating and paleomagnetic record from Trindade Island and stratigraphic implications. Quaternary Geochronology. 2024;81:101518.
114. Milanese FN, Rapalini AE, Sagripanti L, Geuna S, Dekkers MJ, Feo R, et al. New and revised paleomagnetic data from the southern central andes: Testing tectonic rotations. Journal of South American Earth Sciences. 2023;124:104220.
115. Moncinhatto TR, de Oliveira WP, Haag MB, Hartmann GA, Savian JF, Poletti W, et al. Palaeosecular variation in Northern Patagonia recorded by 0–5 Ma Caviahue–Copahue lava flows. Geophysical Journal International. 2023;234(3):1640-54.
116. Muxworthy AR, Riishuus MS, Supakulopas R, Niocaill CM, Barfod DN, Døssing A, et al. The palaeomagnetic field recorded in Eyjafjarðardalur basalts (2.6–8.0 Ma), Iceland: are inclination-shallowing corrections necessary in time-averaged field analysis? Geophysical Journal International. 2024;238(2):764-82.
117. Chi Y, Lhuillier F. Paleomagnetic secular variation of early middle miocene volcanics from Vogelsberg (Germany). Journal of Geophysical Research: Solid Earth. 2025;130(4):e2024JB031007.
118. Pivarunas AF, Avery MS, Hagstrum JT, Bennett SE, Calvert AT. New paleomagnetic constraints on the eruption timing, stratigraphy, and post-emplacement deformation of the Picture Gorge Basalt within the Columbia River Basalt Group. Journal of Geophysical Research: Solid Earth. 2025;130(3):e2024JB030728.
119. Murray M, Biggin A, Paterson G, Tully A, Urbani S. Paleomagnetism of the British Paleogene Igneous Province: paleosecular variation and paleointensity inversion from the Skye dyke swarm. Authorea Preprints. 2025.
120. Venkateshwarlu M, Satyakumar A. Paleomagnetism of mafic dykes in South Rewa Basin, India: Constraints to extension of Deccan volcanism. Geosystems and Geoenvironment. 2024;3(3):100292.
121. Ernesto M, Endale T, Batezelli A, Saad AR. Magnetostratigraphic and sedimentological insights into the Late Campanian Uberaba Formation of the Bauru Group, southeast Brazil. Journal of South American Earth Sciences. 2025;151:105252.
122. Ernesto M, Raposo MIB. The Late Cretaceous alkaline magmatism in the SE Brazilian coast: new paleomagnetic data and age constraints. Brazilian Journal of Geology. 2023;53(2):e20220061.
123. Lhuillier F, Lebedev I, Tikhomirov P, Pavlov V. High-latitude geomagnetic secular variation at the end of the cretaceous normal superchron recorded by volcanic flows from the Okhotsk-Chukotka volcanic belt. Journal of Geophysical Research: Solid Earth. 2024;129(1):e2023JB027550.
124. Globerman BR, Irving E. Mid-Cretaceous paleomagnetic reference field for North America: Restudy of 100 Ma intrusive rocks from Arkansas. Journal of Geophysical Research: Solid Earth. 1988;93(B10):11721-33.

125. Dembo N, Kraus E, Seliverstov I, Weissman G, Granot R. Geomagnetic field behaviour during the early cretaceous normal superchron from palaeomagnetic analysis of the Ramon Volcanics, Israel. Geophysical Journal International. 2022;231(3):1982-95.
126. Raposo MIB, Pescarini T, Guimaraes LF, Esteves MC. New magnetostratigraphy constrains in the southern Paraná magmatic province (Herveiras and Gramado Xavier areas), Rio Grande do Sul state, South Brazil: Implications for the timing between volcanic sources. Journal of South American Earth Sciences. 2023;126:104327.
127. Llanos MPI, Kietzmann DA, Trindade RI, do Carmo JA, Brandt D, Rodriguez-Pinto JP. Magnetostratigraphy and cyclostratigraphy of the Vaca Muerta Formation (Upper Jurassic–Lower Cretaceous) at Puerta Curaco, Neuquén, Argentina. Cretaceous Research. 2026;181:106273.
128. Prasad JN. Paleomagnetism of the Mesozoic lamprophyre dikes in north-central Newfoundland: Memorial University of Newfoundland; 1981.
129. Moreira G, Ernesto M, De Min A, Marzoli A, Machado FB, Vasconcellos EMG, et al. Paleomagnetism of the Penatecaua magmatism: The CAMP intrusive rocks in the Amazonas Basin, northern Brazil. Physics of the Earth and Planetary Interiors. 2023;342:107075.
130. Hounslow MW, Gallois R. Magnetostratigraphy of the Mercia Mudstone Group (Devon, UK): implications for regional relationships and chronostratigraphy in the Middle to Late Triassic of Western Europe. Journal of the Geological Society. 2023;180(4):jgs2022-173.
131. Hounslow MW, McIntosh G. Magnetostratigraphy of the Sherwood Sandstone Group (Lower and Middle Triassic), south Devon, UK: detailed correlation of the marine and non-marine Anisian. Palaeogeography, Palaeoclimatology, Palaeoecology. 2003;193(2):325-48.
132. Nawrocki J, Szulc J. The Middle Triassic magnetostratigraphy from the Peri-Tethys basin in Poland. Earth and Planetary Science Letters. 2000;182(1):77-92.
133. Eliseev A, Metelkin D, Abashev V, Mikhaltsov N, Vinogradov E, Bragin VY. Paleomagnetism of the Abinskaya Group of the Kuznetsk Depression (southern Siberia)–Implications for the evolution of the Siberian Large Igneous Province at the Permian–Triassic boundary. Russian Geology and Geophysics. 2024;65(4):475-90.
134. Weissbrodt V. Paleomagnetism of late Paleozoic basins of the Moroccan Meseta and the Western High Atlas: lmu; 2024.
135. Foster J, Symons D. Defining a paleomagnetic polarity pattern in the Monteregian intrusives. Canadian Journal of Earth Sciences. 1979;16(9):1716-25.
136. Theveniaut H, Besse J, Edel J, Westphal M, Duringer P. A Middle-Triassic paleomagnetic pole for the Eurasian plate from Heming (France). Geophysical Research Letters. 1992;19(8):777-80.
137. Mitchell RN, Zhang N, Salminen J, Liu Y, Spencer CJ, Steinberger B, et al. The supercontinent cycle. Nature Reviews Earth & Environment. 2021;2(5):358-74.
138. Nance RD, Murphy JB, Santosh M. The supercontinent cycle: a retrospective essay. Gondwana Research. 2014;25(1):4-29.
139. van der Meer DG, Torsvik TH, Spakman W, van Hinsbergen DJJ, Amaru ML. Intra-Panthalassa Ocean subduction zones revealed by fossil arcs and mantle structure. Nature Geoscience. 2012;5(3):215-9. doi: 10.1038/ngeo1401.
140. van de Lagemaat SH, Cao L, Asis J, Advokaat E, Mason P, Dekkers MJ, et al. Causes of Late Cretaceous subduction termination below South China and Borneo: Was the Proto-South China Sea underlain by an oceanic plateau? Geoscience Frontiers. 2024;15:101752.

141. Sigloch K, Mihalynuk MG. Intra-oceanic subduction shaped the assembly of Cordilleran North America. Nature. 2013;496(7443):50-6. Epub 2013/04/05. doi: 10.1038/nature12019. PubMed PMID: 23552944.
142. Fuston S, Wu J, Colli L. Cretaceous collision reconciles western North American tectonics with deep mantle slabs. In: Gordon SM, Miller RB, Rusmore ME, Tikoff B, editors. Jurassic–Paleogene Tectonic Evolution of the North American Cordillera. 565: Geological Society of America Special Paper; 2025.
143. Pindell J, Dewey JF. Permo-Triassic reconstruction of western Pangea and the evolution of the Gulf of Mexico/Caribbean region. Tectonics. 1982;1(2):179-211.
144. Pindell JL, Kennan L. Tectonic evolution of the Gulf of Mexico, Caribbean and northern South America in the mantle reference frame: an update. Geological Society, London, Special Publications. 2009;328(1):1.-55. doi: 10.1144/sp328.1.
145. Andjić G, Escuder-Viruete J, Baumgartner-Mora C, Baumgartner PO, Mitchell SF, Caron M, et al. Sedimentary record of arc-continent collision along Mesozoic SW North America (Siuna belt, Nicaragua). Tectonics. 2019;38(12):4399-425.
146. Mortimer N, Campbell HJ, Tulloch AJ, King PR, Stagpoole VM, Wood RA, et al. Zealandia: Earth's hidden continent. GSA today. 2017;27(3):27-35.
147. Schellart WP, Lister GS, Toy VG. A Late Cretaceous and Cenozoic reconstruction of the Southwest Pacific region: Tectonics controlled by subduction and slab rollback processes. Earth-Science Reviews. 2006;76(3-4):191-233. doi: 10.1016/j.earscirev.2006.01.002.
148. Hall R. Cenozoic geological and plate tectonic evolution of SE Asia and the SW Pacific: computer-based reconstructions, model and animations. Journal of Asian Earth Sciences. 2002;20:353-431.
149. Zahirovic S, Seton M, Müller RD. The Cretaceous and Cenozoic tectonic evolution of Southeast Asia. Solid Earth. 2014;5(1):227-73. doi: 10.5194/se-5-227-2014.
150. Boschman LM, Molina Garza RS, Langereis CG, van Hinsbergen DJJ. Paleomagnetic constraints on the kinematic relationship between the Guerrero terrane (Mexico) and North America since Early Cretaceous time. GSA Bulletin. 2018;130:1131-42. doi: 10.1130/b31916.1.
151. Martini M, Solari L, López-Martínez M. Correlating the Arperos Basin from Guanajuato, central Mexico, to Santo Tomás, southern Mexico: Implications for the paleogeography and origin of the Guerrero terrane. Geosphere. 2014;10(6):1385-401. doi: 10.1130/ges01055.1.
152. Tikoff B, Housen B, Maxson J, Nelson E, Trevino S, Shipley T. Hit-and-run model for Cretaceous–Paleogene tectonism along the western margin of Laurentia. 2023.
153. Clennett EJ, Sigloch K, Mihalynuk MG, Seton M, Henderson MA, Hosseini K, et al. A quantitative tomotectonic plate reconstruction of western North America and the eastern Pacific basin. Geochemistry, Geophysics, Geosystems. 2020;21(8):e2020GC009117.
154. Wakabayashi J, Reyes JR. Spatiotemporal framework of the Franciscan Complex, California, bearing on the continuity of subduction and the accommodation of oblique convergence. In: Riggs N, Putirka K, Wakabayashi J, editors. The Virtue of Fieldwork in Volcanology, Sedimentology, Structural Geology, and Tectonics—Celebrating the Career of Cathy Busby. 563: Geological Society of America Special Paper; 2025.
155. Nokleberg WJ, Parfenov LM, Monger JWH, Norton IO, Khanchuk A, Stone DB, et al. Phanerozoic tectonic evolution of the Circum-North Pacific: US Department of the Interior, US Geological Survey; 2000.

156. Andjić G, Vaes B, van de Lagemaat SH, Boschman LM, Dekkers MJ, Johnston ST, et al. Paleolatitudinal Drift and Major Rotation of the Wrangellia Superterrane in the Mesozoic: A Signal of East-Panthalassa Plate Motion? Tectonics. 2025;44(1):e2024TC008337.
157. Johnston ST. The Great Alaskan Terrane Wreck: reconciliation of paleomagnetic and geological data in the northern Cordillera. Earth and Planetary Science Letters. 2001;193(3-4):259-72.
158. Schellart W, Strak V, Beniest A, Duarte J, Rosas F. Subduction invasion polarity switch from the Pacific to the Atlantic Ocean: A new geodynamic model of subduction initiation based on the Scotia Sea region. Earth-Science Reviews. 2022:104277.
159. Şengör AMC. Plate tectonics and orogenic research after 25 years: A Tethyan perspective. Earth-Science Reviews. 1990;27(1-2):1-201.
160. Cawood PA, Merdith AS, Murphy JB. Syn-emplacement ophiolites and relationship to supercontinent cycle. Earth and Planetary Science Letters. 2024;641:118810.
161. Wan B, Wu F, Chen L, Zhao L, Liang X, Xiao W, et al. Cyclical one-way continental rupture-drift in the Tethyan evolution: Subduction-driven plate tectonics. Science China Earth Sciences. 2019;62:2005–16.
162. Gutiérrez-Alonso G, Fernández-Suárez J, Weil AB, Brendan Murphy J, Damian Nance R, Corfú F, et al. Self-subduction of the Pangaean global plate. Nature Geoscience. 2008;1(8):549-53. doi: 10.1038/ngeo250.
163. Gibbons AD, Barckhausen U, van den Bogaard P, Hoernle K, Werner R, Whittaker JM, et al. Constraining the Jurassic extent of Greater India: Tectonic evolution of the West Australian margin. Geochemistry Geophysics Geosystems. 2012;13. doi: 10.1029/2011gc003919.
164. Kravchinsky VA, Cogné J-P, Harbert WP, Kuzmin MI. Evolution of the Mongol-Okhotsk Ocean as constrained by new palaeomagnetic data from the Mongol-Okhotsk suture zone, Siberia. Geophysical Journal International. 2002;148(1):34-57.
165. Gaina C, Torsvik TH, van Hinsbergen DJJ, Medvedev S, Werner SC, Labails C. The African Plate: A history of oceanic crust accretion and subduction since the Jurassic. Tectonophysics. 2013;604:4-25. doi: 10.1016/j.tecto.2013.05.037.
166. Frisch W. Tectonic progradation and plate tectonic evolution of the Alps. Tectonophysics. 1979;60(3-4):121-39.
167. Vissers RLM, van Hinsbergen DJJ, Meijer PT, Piccardo GB. Kinematics of Jurassic ultra-slow spreading in the Piemonte Ligurian ocean. Earth and Planetary Science Letters. 2013;380:138-50. doi: 10.1016/j.epsl.2013.08.033.
168. Şengör AMC, Yilmaz Y. Tethyan evolution of Turkey: A plate tectonic approach. Tectonophysics. 1981;75(3):181-241. doi: https://doi.org/10.1016/0040-1951(81)90275-4.
169. Şengör AMC. The Cimmeride orogenic system and the tectonics of Eurasia. Geological Society of America Special Paper. 1984;195:82.
170. Barrier E, Vrielynck B. MEBE atlas of paleotectonic maps of the Middle East: Commission for the geological map of the world. Paris; 2008.
171. Dercourt J, et al., Zonenshain LP, Ricou LE, Kazmin VG, Le Pichon X, et al. Geological evolution of the Tethys belt from the Atlantic to the Pamirs since the Lias. Tectonophysics. 1986;123(1-4):241-315.
172. Stampfli G, Marcoux J, Baud A. Tethyan margins in space and time. Palaeogeography, Palaeoclimatology, Palaeoecology. 1991;87(1-4):373-409.
173. Stampfli GM, Hochard C. Plate tectonics of the Alpine realm. Geological Society, London, Special Publications. 2009;327(1):89-111. doi: 10.1144/sp327.6.

174. Handy MR, Ustaszewski K, Kissling E. Reconstructing the Alps–Carpathians–Dinarides as a key to understanding switches in subduction polarity, slab gaps and surface motion. International Journal of Earth Sciences. 2015;104(1):1-26.
175. Şengör AMC. Tectonics of the Tethysides: Orogenic Collage Development in a Collisional Setting. Annual Review of Earth and Planetary Sciences. 1987;15(1):213-44. doi: 10.1146/annurev.ea.15.050187.001241.
176. Stampfli GM, Borel G. A plate tectonic model for the Paleozoic and Mesozoic constrained by dynamic plate boundaries and restored synthetic oceanic isochrons. Earth and Planetary Science Letters. 2002;196(1):17-33.
177. Muttoni G, Mattei M, Balini M, Zanchi A, Gaetani M, Berra F. The drift history of Iran from the Ordovician to the Triassic. Geological Society, London, Special Publications. 2009;312(1):7-29. doi: 10.1144/sp312.2.
178. Stern RJ, Moghadam HS, Pirouz M, Mooney W. The geodynamic evolution of Iran. Annual Review of Earth and Planetary Sciences. 2021;49(1):9-36.
179. GholamiZadeh P, Wan B, Garzanti E, Hu X, Esmaeili R, Ebrahimi M. Collision Timing and Provenance Shifts from the Late Oligocene to Middle Miocene in the Southeasternmost Zagros Orogen. Scientific Reports. 2025;15(1):6023.
180. Zhang K-J, Zhang Y-X, Li B, Zhu Y-T, Wei R-Z. The blueschist-bearing Qiangtang metamorphic belt (northern Tibet, China) as an in situ suture zone: Evidence from geochemical comparison with the Jinsa suture. Geology. 2006;34(6):493-6.
181. Metcalfe I. Multiple Tethyan ocean basins and orogenic belts in Asia. Gondwana Research. 2021;100:87-130.
182. Yin A, Harrison TM. Geologic evolution of the Himalayan-Tibetan orogen. Annual Review of Earth and Planetary Sciences. 2000;28(1):211-80.
183. Kapp P, DeCelles PG. Mesozoic–Cenozoic geological evolution of the Himalayan-Tibetan orogen and working tectonic hypotheses. American Journal of Science. 2019;319(3):159-254.
184. Garzanti E, Le Fort P, Sciunnach D. First report of Lower Permian basalts in South Tibet: tholeiitic magmatism during break-up and incipient opening of Neotethys. Journal of Asian Earth Sciences. 1999;17(4):533-46.
185. Li Z, Ding L, Lippert PC, Song P, Yue Y, van Hinsbergen DJJ. Paleomagnetic constraints on the Mesozoic drift of the Lhasa terrane (Tibet) from Gondwana to Eurasia. Geology. 2016;44(9):727-30. doi: 10.1130/g38030.1.
186. Gartrell A, Keep M, van der Riet C, Paterniti L, Ban S, Lang S. Hyperextension and polyphase rifting: Impact on inversion tectonics and stratigraphic architecture of the North West Shelf, Australia. Marine and Petroleum Geology. 2022;139:105594.
187. Veevers J, Powell CM, Roots S. Review of seafloor spreading around Australia. I. Synthesis of the patterns of spreading. Australian journal of earth sciences. 1991;38(4):373-89.
188. Advokaat EL, Bongers MLM, Rudyawan A, BouDagher-Fadel MK, Langereis CG, van Hinsbergen DJJ. Early Cretaceous origin of the Woyla Arc (Sumatra, Indonesia) on the Australian plate. Earth and Planetary Science Letters. 2018;498:348-61.
189. Hu X, Jansa L, Chen L, Griffin WL, O'Reilly SY, Wang J. Provenance of Lower Cretaceous Wölong volcaniclastics in the Tibetan Tethyan Himalaya: Implications for the final breakup of eastern Gondwana. Sedimentary Geology. 2010;223(3-4):193-205.
190. Licht A, Dupont-Nivet G, Westerweel J, Win Z, Guihou A, Deschamps P, et al. The missing arcs of the India-Asia collision. Gondwana Research. 2025.

191. Whittaker JM, Williams SE, Halpin JA, Wild TJ, Stilwell JD, Jourdan F, et al. Eastern Indian Ocean microcontinent formation driven by plate motion changes. Earth and Planetary Science Letters. 2016;454:203-12. doi: 10.1016/j.epsl.2016.09.019.
192. Torsvik TH, Amundsen H, Hartz EH, Corfu F, Kusznir N, Gaina C, et al. A Precambrian microcontinent in the Indian Ocean. Nature Geoscience. 2013;6(3):223-7. doi: 10.1038/ngeo1736.
193. An W, Hu X, Garzanti E. Discovery of Upper Cretaceous Neo-Tethyan trench deposits in south Tibet (Luogangcuo Formation). Lithosphere. 2018;10(3):446-59.
194. van Hinsbergen DJJ. Indian Plate paleogeography, subduction, and horizontal underthrusting below Tibet: paradoxes, controvercies, and opportunities. National Science Review. 2022;9(8):nwac074. doi: https://doi.org/10.31223/X54M0V.
195. Zhu M, Wakabayashi J, Pastor-Galán D, Zhang F, Ganbat A, Miao L, et al. Large-scale Permo-Triassic back-arc extensions of the Mongol-Okhotsk Ocean. Bulletin. 2023;135(9-10):2563-74.
196. Han Y, Zhao G, Cawood PA, Sun M, Eizenhöfer PR, Hou W, et al. Tarim and North China cratons linked to northern Gondwana through switching accretionary tectonics and collisional orogenesis. Geology. 2016;44(2):95-8.
197. Cawood PA, Wang Y, Xu Y, Zhao G. Locating South China in Rodinia and Gondwana: A fragment of greater India lithosphere? Geology. 2013;41(8):903-6.
198. Hacker BR, Ratschbacher L, Liou J. Subduction, collision and exhumation in the ultrahigh-pressure Qinling-Dabie orogen. 2004.
199. Heath JA, Cooper N, Upchurch P, Mannion PD. Accounting for sampling heterogeneity suggests a low paleolatitude origin for dinosaurs. Current Biology. 2025;35:941-53.
200. Uhen MD, Allen B, Behboudi N, Clapham ME, Dunne E, Hendy A, et al. Paleobiology database user guide version 1.0. PaleoBios. 2023;40(11).
201. Scotese CR, Bambach RK, Barton C, Van der Voo R, Ziegler AM. Paleozoic base maps. The Journal of Geology. 1979;87(3):217-77.
202. Scotese CR, Sager WW. Mesozoic and Cenozoic plate reconstructions. Tectonophysics. 1989;155:27-48.
203. Wright N, Zahirovic S, Müller RD, Seton M. Towards community-driven paleogeographic reconstructions: integrating open-access paleogeographic and paleobiology data with plate tectonics. Biogeosciences. 2013;10(3):1529-41. doi: 10.5194/bg-10-1529-2013.
204. Torsvik TH, van der Voo R. Refining Gondwana and Pangea palaeogeography: estimates of Phanerozoic non-dipole (octupole) fields. Geophysical Journal International. 2002;151(3):771-94.
205. Tetley MG. Constraining Earth's plate tectonic evolution through data mining and knowledge discovery 2018.
206. Van der Voo R. The reliability of paleomagnetic data. Tectonophysics. 1990;184(1):1-9.
207. Torsvik T, Steinberger B, Cocks L, Burke K. Longitude: Linking Earth's ancient surface to its deep interior. Earth and Planetary Science Letters. 2008;276(3-4):273-82. doi: 10.1016/j.epsl.2008.09.026.
208. Roy K, Jablonski D, Valentine JW, Rosenberg G. Marine latitudinal diversity gradients: tests of causal hypotheses. Proceedings of the national Academy of Sciences. 1998;95(7):3699-702.

209. Brodie JF, Mannion PD. The hierarchy of factors predicting the latitudinal diversity gradient. Trends in Ecology & Evolution. 2023;38(1):15-23.
210. Brayard A, Escarguel G, Bucher H. Latitudinal gradient of taxonomic richness: combined outcome of temperature and geographic mid-domains effects? Journal of Zoological Systematics and Evolutionary Research. 2005;43(3):178-88.
211. Yasuhara M, Hunt G, Dowsett HJ, Robinson MM, Stoll DK. Latitudinal species diversity gradient of marine zooplankton for the last three million years. Ecology letters. 2012;15(10):1174-9.
212. Varela S, González-Hernández J, Sgarbi LF, Marshall C, Uhen MD, Peters S, et al. paleobioDB: an R package for downloading, visualizing and processing data from the Paleobiology Database. Ecography. 2015;38(4):419-25.
213. Cox A. Latitude dependence of the angular dispersion of the geomagnetic field. Geophysical Journal International. 1970;20(3):253-69.
214. Deenen MHL, Langereis CG, van Hinsbergen DJJ, Biggin AJ. Geomagnetic secular variation and the statistics of palaeomagnetic directions. Geophysical Journal International. 2011;186(2):509-20. doi: 10.1111/j.1365-246X.2011.05050.x.
215. Pisarevsky S. New edition of the global paleomagnetic database. Wiley Online Library; 2005.
216. Pisarevsky S, Li Z, Tetley M, Liu Y, Beardmore J. An updated internet-based global paleomagnetic database. Earth-Science Reviews. 2022;235:104258.
217. Cromwell G, Johnson CL, Tauxe L, Constable C, Jarboe NA. A global data set for 0–10 Ma time-averaged field and paleosecular variation studies. Geochemistry, Geophysics, Geosystems. 2018;19:1533-58.